Analysis of Snow Multi-Bands and Their Environments with High-Resolution Idealized Simulations

Nicholas M. Leonardo and Brian A. Colle

School of Marine and Atmospheric Sciences, Stony Brook University, Stony Brook, NY

Submitted to the Mon. Wea. Rev.

14 September 2023

Revised

1 January 2024

*Corresponding author address:

Dr. Nicholas M. Leonardo

School of Marine and Atmospheric Sciences

Stony Brook University / SUNY

Stony Brook, NY 11794-5000

Email: Nicholas.leonardo@stonybrook.edu

Abstract

Nested idealized baroclinic wave simulations at 4-km and 800-m grid spacing are used to analyze the precipitation structures and their evolution in the comma head of a developing extratropical cyclone. After the cyclone spins up by hour 120, snow multi-bands develop within a wedge-shaped region east of the near-surface low center within a region of 700-500-hPa potential and conditional instability. The cells deepen and elongate northeastward as they propagate north. There is also an increase in 600-500-hPa southwesterly vertical wind shear prior to band development. The system stops producing bands 12 hours later as the differential moisture advection weakens, and the instability is depleted by the convection.

Sensitivity experiments are run in which the initial stability and horizontal temperature gradient of the baroclinic wave are adjusted by 5-10%. A 10% decrease in initial instability results in less than half the control run potential instability by 120 h and the cyclone fails to produce multi-bands. Meanwhile, a 5% decrease in instability delays the development of multi-bands by 18 h. Meanwhile, decreasing the initial horizontal temperature gradient by 10% delays the growth of vertical shear and instability, corresponding to multi-bands developing 12-18 hours later. Conversely, increasing the horizontal temperature gradient by 10% corresponds to greater vertical shear, resulting in more prolific multi-band activity developing ~12 hours earlier. Overall, the relatively large changes in band characteristics over a ~12-hour period (120-133 h) and band evolutions for the sensitivity experiments highlight the potential predictability challenges.

Significance Statement

The purpose of this study is to better understand the mechanisms that organize winter storm precipitation into multi-banded structures. These small-scale bands are difficult to predict and can greatly impact snowfall forecasts. The analysis is performed on a conceptual low pressure system in a numerical model to systematically isolate the roles of different ambient conditions. The results emphasize that environments with instability (e.g., where temperature and moisture decrease with height) and wind shear (winds increase with height) favor the development of banded structures as the system intensifies. Decreasing the instability by 10% suppresses band development, while increasing (decreasing) the horizontal temperature change across the system by up to 10% corresponds to the bands developing up to 12 h earlier (later).

1. Introduction:

a. Background.

Snowbands within the comma head of extratropical cyclones cause locally enhanced snow accumulations, ice accretion on tree limbs and powerlines, and travel hazards. The small-scale nature of these bands makes them difficult to forecast. Much of the past work has focused on primary (single) snowbands with widths typically on the order of tens of kilometers and lengths over 200 km (Novak et al. 2004, 2008, 2009, 2010; Kenyon 2013). These bands are often associated with well-defined mid-level frontogenesis and weak stability, potential instability, or conditional instability (Novak et al. 2008, 2010; Ganetis et al. 2018). Less attention has been given to multi-bands. While multi-bands are generally defined as two or more elongated enhanced features in reflectivity, the criteria vary between studies. Novak et al. (2004) defined multi-bands as being 5-20 km wide with intensities >10 dBZ over the background reflectivity maintained for >2 hours. Kenyon et al. (2013) defined bands as having aspect ratios >4:1 and reflectivity >10 dBZ over the background for >3 hours.

A few mechanisms have been proposed for the development of multi-bands. Early studies emphasized that frontogenesis in an environmental with conditional symmetric instability (CSI) is associated with multi-bands (Xu 1992; Nicosia and Grumm 1999). Conditional instability (CI) or CSI has been shown to occur more often in multi-bands than single-band cases (Novak et al., 2010; Ganetis et al. 2018). However, CSI is not a necessary condition in multi-band genesis (Novak et al. 2004; Connelly and Colle 2019), with some cases occurring in a shallow layer of CI instead (Shields et al. 1991). Ganetis et al. (2018) completed a band climatology over 20 winters and showed that many small-scale bands were not associated with CSI or frontogenesis. Rather, there was CI or potential instability (PI) for many of these bands, and the lifting mechanism to trigger the bands was unclear. Previous work has also suggested that gravity waves within a stable ducted layer may provide the forcing mechanism for multi-bands (Uccellini and Koch 1987; Plougonven and Zhang 2014; Kawashima 2016; Rauber et al. 2017). Lastly, vertical wind shear at low-levels can stretch the fallout from generating cells aloft into banded features (Evans et al. 2005; Rosenow et al. 2014; Keeler et al. 2016a,b).

b. Motivation

There have been many previous investigations of primary bands using case studies, which have been relatively well simulated and validated with observations (Novak et al. 2004, 2008, 2010; Kenyon 2013; Baxter and Schumacher 2017). In contrast, few studies have analyzed multi-band cases, which have been more difficult to simulate (Connelly and Colle 2019).

Given the complexity of case studies, idealized simulations have been used to more systematically investigate the processes associated with precipitation bands. For example, Norris et al. 2014, 2017 used the idealized baroclinic wave setup in Weather Research and Forecasting Model (WRF; Skamarock et al. 2008) to examine precipitation bands and analyze their sensitivity to surface enthalpy and momentum fluxes. However, they focused on the cold frontal region in later stages of the system, rather than the comma head region where snow bands are traditionally found.

As further motivation for the multi-bands in this idealized modeling study, Figure 1 shows two multi-banding events from 16 January 2022 and 12 February 2023 using the Multi-Radar Multi-Sensor (MRMS; Zhang et al. 2016) composite reflectivity and the high-resolution rapid refresh analysis (HRRR; Dowell et al. 2022). The bands are located to the northeast of the cyclone center (Fig. 1a,c), similar to the multi-band climatology in Novak et al. (2004) and Ganetis et al. (2018). The individual bands are 100-200 km in length, stretching southwest-to-northeast in orientation and propagating northward around the low center. The "wedge" of bands for each case only lasted 3-9 hours, after which the convection east of the low center becomes more sparse and less organized (Figs. 1b,d). The short duration of these bands highlights some of the predictability challenges.

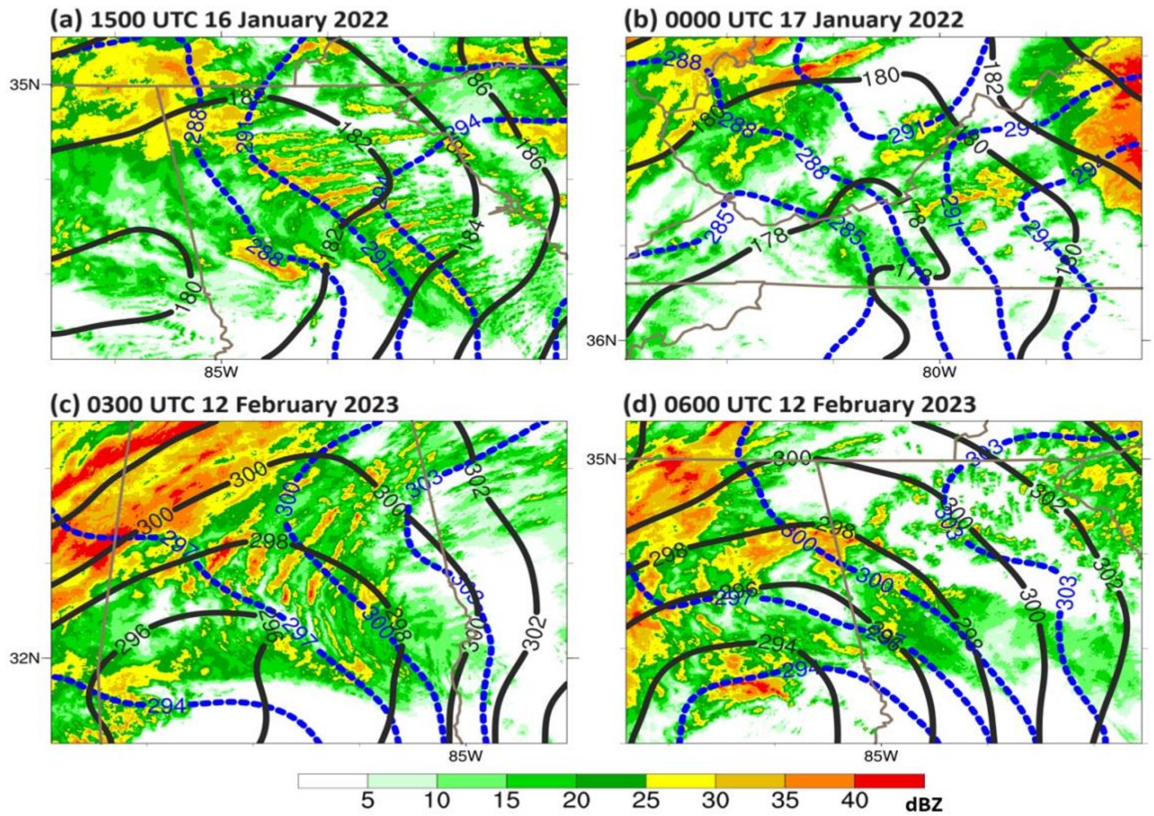

Figure 1: MRMS composite reflectivity (shaded), and HRRR analysis 800-hPa geopotential heights (black contour; every 2 dam) and potential temperature (blue dash; every 2 K), valid at (a) 1500 UTC 16 January 2022 and (b) 0000 UTC 17 January 2022. MRMS composite reflectivity (shaded), and HRRR analysis 700-hPa geopotential heights (black contour; every 2 dam) and potential temperature (blue contour; every 2 K), valid at (a) 0300 UTC 12 February 2023 and (b) 0600 UTC 12 February 2023.

This study seeks to investigate the band structures and the environmental factors associated with their development using nested runs of an idealized baroclinic wave model down to 800 m grid spacing. These simulations will help address the following questions:

- How do the precipitation structures in the comma head evolve as the cyclone develops?
- How are changes in the ambient frontogenesis (forcing), vertical shear, and instability around the cyclone related to changes in the precipitation structures?
- How do small changes in the initial stability and temperature gradient of the baroclinic wave affect subsequent band development?

The remainder of this paper is organized as follows. Section 2 will highlight the setup of the model and methodology. Section 3 will analyze the structure and evolution of the snow bands, while section 4 will assess the development of the large-scale environment associated with the bands. Section 5 will analyze the sensitivity of the simulated bands to changes in the initial stability and temperature gradient. Summary and conclusions will be presented in the final section. A follow-up paper will investigate more of the mesoscale processes within the bands in these simulations.

2. **Data and Methods**

This study uses the idealized baroclinic-wave setup in version 3.4.1 of the Advanced Research core of the Weather Research and Forecasting Model (ARW-WRF; Skamarock et al. 2008). The model version and methodology are the same as Norris et al. (2014), except that our inner nests are centered on the comma head region of the low. The model is initialized with a 60-70-$m \cdot s^{-1}$ zonal jet centered at ~300 hPa (Fig. 3a), which Rotunno et al. (2004) derived by inverting a baroclinically unstable PV distribution in the y-z plane. The initial moisture is prescribed by a relative humidity profile that linearly decreases from 70% at the surface to 10% at 8 km AGL. Impacts of the setup on band development are shown in section 5.

The outer domain is 8000-by-8000 km in size, with 100-km grid spacing and periodic boundary conditions in the x-direction. The zonal extent of the domain is twice the wavelength of the most unstable mode in the initial jet, such that two nearly identical baroclinic waves develop. These waves propagate from left to right and take more than 72 h to develop a surface low (Fig. 2a through 2c). Inner one-way nests with grid spacing of 20 km and 4 km are added at 108 h to capture the left wave in Fig. 2c after it reenters the western edge of the 100-km grid. The one-way nesting enables an assessment of the sensitivity to horizontal grid spacing. An 800-m nest is then added between 114 h and 132 h during the peak band activity to the northeast of the low. All grids have 64 vertical levels from the surface up to 16 km.

The WRF setup uses an f-plane approximation, the Thompson microphysics scheme (Thompson et al. 2008), and the Yonsei University boundary layer scheme (Hong et al. 2006). The Kain-Fritsch convection scheme is used only in the outer 100-km and 20-km grids.

Following Norris et al. (2014, 2017), surface fluxes are enabled by setting the sea surface temperature to the initial temperature of the lowest model level, and the surface roughness length is set to 0.2 mm.

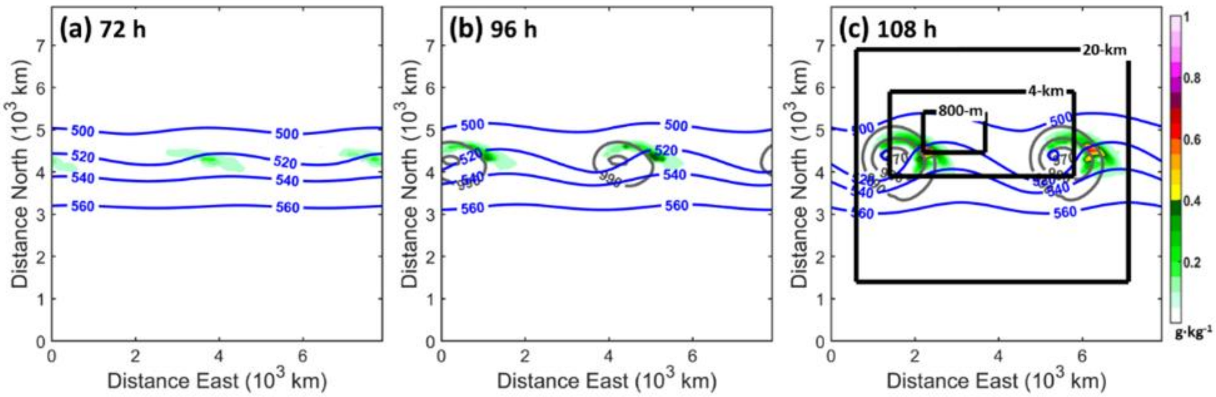

Figure 2: 500-hPa geopotential heights (blue contours; every 20 dam), sea level pressure (grey contours; every 10 hPa below 1000 hPa), and 700-hPa snow and ice mixing ratios (shaded in g kg^{-1}) for the 100-km control domain at (a) 72 h, (b) 96 h, and (c) 108 h. The boxes in (c) indicate the positions of the inner 20-km (d02), 4-km (d03), and 800-m (d04) nests.

3. Idealized Band Evolution

a. Band Structures

Three phases in the banding activity are identified throughout the 4-km control run: genesis, maturity, and decay. The genesis phase (~120-126 h) is when the system begins producing multi-bands, which start as convective cells to the east of the surface low. The mature activity (127-133 h) is defined by when the bands are most intense and numerous, extending to the north the cyclone comma head. Decay (136-140 h) is when the system stops producing well-defined bands. Figure 3 demonstrates the organization of precipitation structures around the low center during these phases. The plots are zoomed-in, with a domain that follows the low center within the 4-km grid. Note that the precipitation within this region north and east of the low is almost entirely snow.

At 111 h, nine hours before the genesis phase, the 295-K isentrope averaged for 700-600 hPa delineates a trough of warm air aloft (e.g., TROWAL, Penner 1955; Galloway 1960; Martin

1998), which is east of the low center enclosed by the 250-dam geopotential height contour (Fig. 3a). The surface pressure of the deepening cyclone center is ~970 hPa (not shown). Linear convective elements are apparent to the north of the TROWAL, but they have aspect ratios less than 4:1 and diminish within the subsequent hour (not shown), such that, following the definitions by Kenyon et al. (2013), they are not considered bands. A more persistent region of convective cells develops to the west of the TROWAL, 100-200 km northwest of point B.

At the start of the genesis phase at 120 h, the cellular convection 200-300 km to the northeast of the surface cyclone fills, forming a "wedge" shape region that extends southeast-to-northwest along the TROWAL (Fig. 3b). As the cells at the tip of the wedge move northwestward from points B to A, they elongate into distinct bands oriented southwest-to-northeast. These bands slowly dissipate as they advance further northward away from the low. The total life cycle of each individual band from its development as a cell to its dissipation is three to six hours. The system continues to generate multiple bands throughout the subsequent 15 to 18 hours. The structure of this "wedge" and bands are similar to the two observed cases shown in Fig. 1.

The multi-band activity to the northeast of the cyclone reaches maturity by 129 h, during which several bands are clearly visible near point A (Fig. 3c). These southwest-northeast orientated bands reach more than 200 km in length and persist more than 500 km north of the low center. The surface pressure of the low center has further deepened to ~963 hPa (not shown). The different stages of the bands' lifecycle are annotated, from the isolated cells near point B (one of which is marked "Cell"), to the deeper embedded convection gaining linear attributes while crossing the middle point between B and A ("Hybrid"), to the discreet elongated bands near A ("Band").

The multi-band activity decays by 138 h (Fig. 3d), at which point the convection broadens and forms a large band along the TROWAL axis. While some embedded linear features are visible, they are much weaker than those over the same area at 129 h, with snow mixing ratios ~40 percent smaller. The bands that were northeast of the low at 129 h have since dissipated without being replaced by new bands from the south. The surface low has since reached its lowest pressure of ~960 hPa (not shown). In the subsequent six hours, the pressure slowly rises, consistent with the low occluding and becoming more disconnected from the warm air to the southeast (not shown).

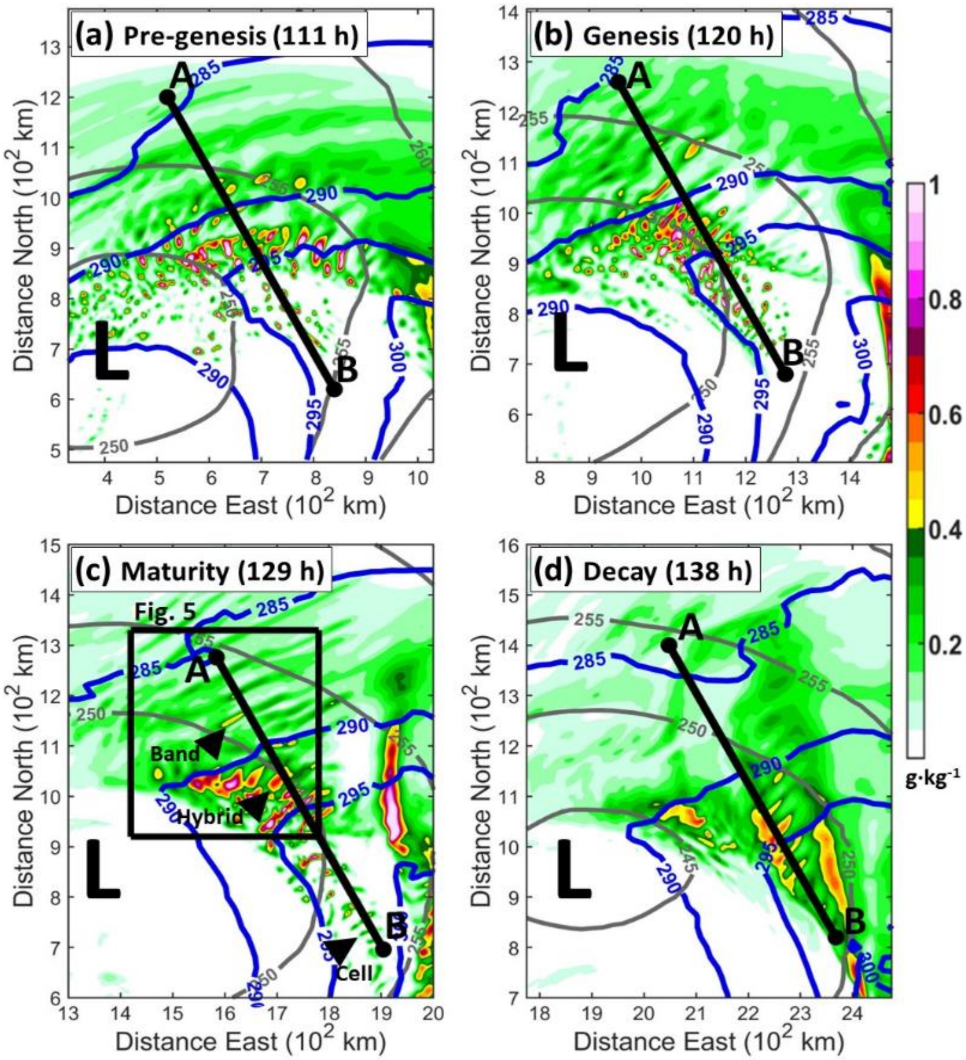

Figure 3: 700-hPa snow and ice mixing ratios (shaded every 0.05 g kg^{-1}), 700-hPa geopotential heights (black contours every 5 dam), and 700-600-hPa potential temperature (blue contours every 5 K) for the 4-km control run at (a) 111 h, (b) 120 h, (c) 129 h, and (d) 138 h. Each tick is 200 km. The position of the 700-hPa low pressure center is marked by an L. The black lines mark the locations of cross-sections taken from A to B in Fig. 4. In (c), the box marks the area that Fig. 5 focuses on, and the stages of band development during the mature phase are annotated with arrows in (c).

The vertical structures of the bands are examined in northwest-to-southeast cross-sections (points A and B in Fig 3). The section is orientated along where the bands start as cells (cell and hybrid region in Fig 4c), and mature and decay (hybrid and band in Fig. 4c) to the northeast of the cyclone. Between the pre-genesis (111 h; Fig. 4a) and genesis (120 h; Fig. 4b) phases, there is an increase in the number of convective plumes (e.g., the three bands with 700-600-hPa snow mixing ratios >0.3 g·kg^{-1} within 150 km from point A in Fig. 4b). These convective structures grow upwards as they move northwest toward point A along the frontal zone. The bands then weaken within ~200 km of point A.

During maturity at 129 h (Fig. 4c), the largest snow mixing ratios develop above 700 hPa, as seen in the three plumes right of the "Hybrid" between 300 and 400 km from point A. The largest upward motion within these plumes is 0.2-0.5 m·s^{-1} and elevated between 650 and 500 hPa. By comparison, the upward motion associated with the three plumes < 100 km from point A is 0.1-0.3 m·s^{-1}. The convective plumes are surrounded by narrow regions of weak subsidence (0.1-0.2 m·s^{-1}) between 650 and 500 hPa (not shown). During the decay phase at 138 h, only several embedded plumes are visible (Fig 4d). The snow and vertical motions associated with these plumes are 30-50% weaker than those at 129 h.

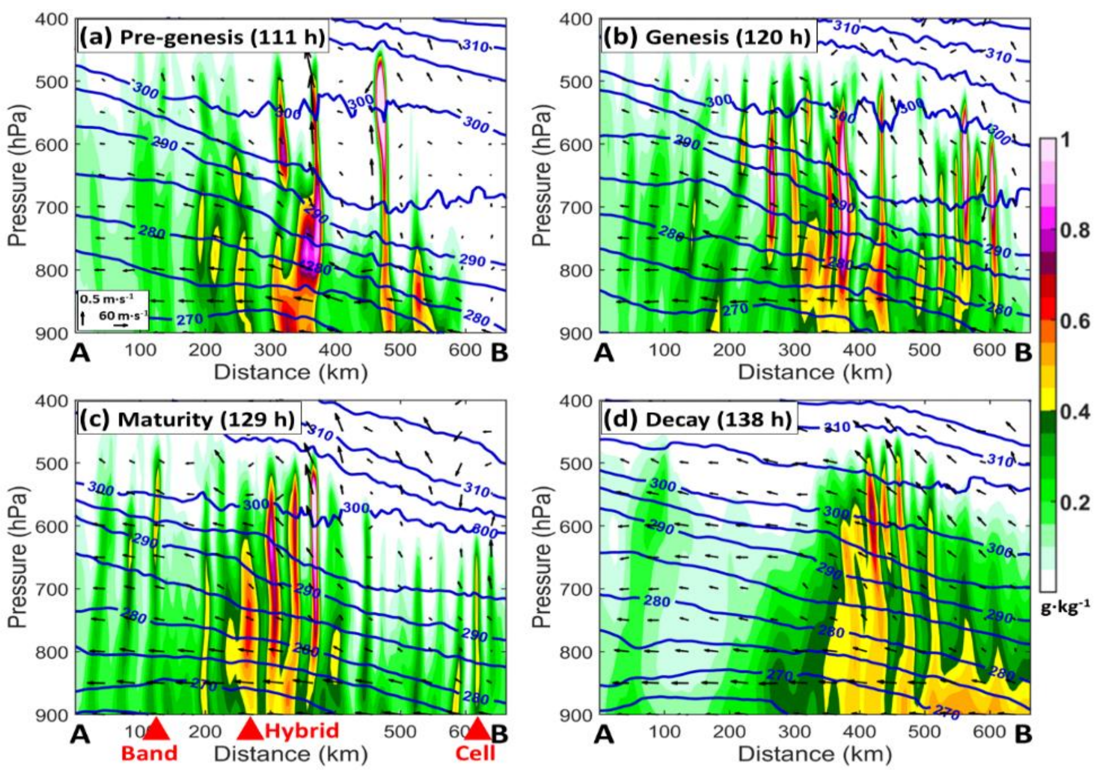

Figure 4: cross-sections of snow and ice mixing ratios (shaded), potential temperature (blue contours; every 5 K), and circulation vectors of the 4-km at (a) 111 h, (b) 120 h, (c) 129 h, and (d) 138 h. The locations of the cross-sections are plotted in Fig. 3. The stages of the bands from Fig. 3c are annotated with arrows.

b. Impact of Resolution and Band Evolution.

To show the impact of horizontal resolution on the band structures, Fig. 5 illustrates the 4-km and 800-m domains during the peak in band activity. The plots are zoomed on the northeast flank of the 700-hPa low and north of the TROWAL (e.g., the black box in Fig 3c), to capture the evolution of bands marked “1”, “2”, and “3”. These bands are among the group northeast of the low at 129 h, with band 3 being the same mature band annotated in Fig. 3c. At 126 h, the three features appear disorganized in the 4-km, embedded within a mass of cellular activity (Fig 5a). The 4-km elongates these features into distinct bands by 129 h (Fig. 5b). Band 3 reaches the greatest intensity and stretches ~60-km from southwest to northeast, as measured by the 0.4-$g \cdot kg^{-1}$ contour (yellow shading) in snow mixing ratios. Through 130 h, the three bands continue to broaden northeastward, though their maximum snow mixing ratios decrease by 20-40% compared to 129 h (Fig. 5c).

These same three bands in the 4-km are similar in the 800-m grid. At 126 h, the 800-m has more linear convective structures embedded north of the TROWAL than the 4-km (Figs. 5a, d). Smaller-scale precipitation features are between the developing bands. However, each of these features persists less than an hour (not shown). By 129 h, the three bands elongate and have a similar intensity as the 4-km grid, with the 0.4-g/kg snow mixing ratio contour around band 3 reaching ~80 km in length (Fig 5e). The bands further broaden by 130 h, while also weakening in amplitude much like in the 4-km (Fig 5f). The bands continue to track northward before completely dissipating ~131.5 h (not shown). Overall, there is little difference in horizontal band structure and evolution between the 4-km and 800-m grids.

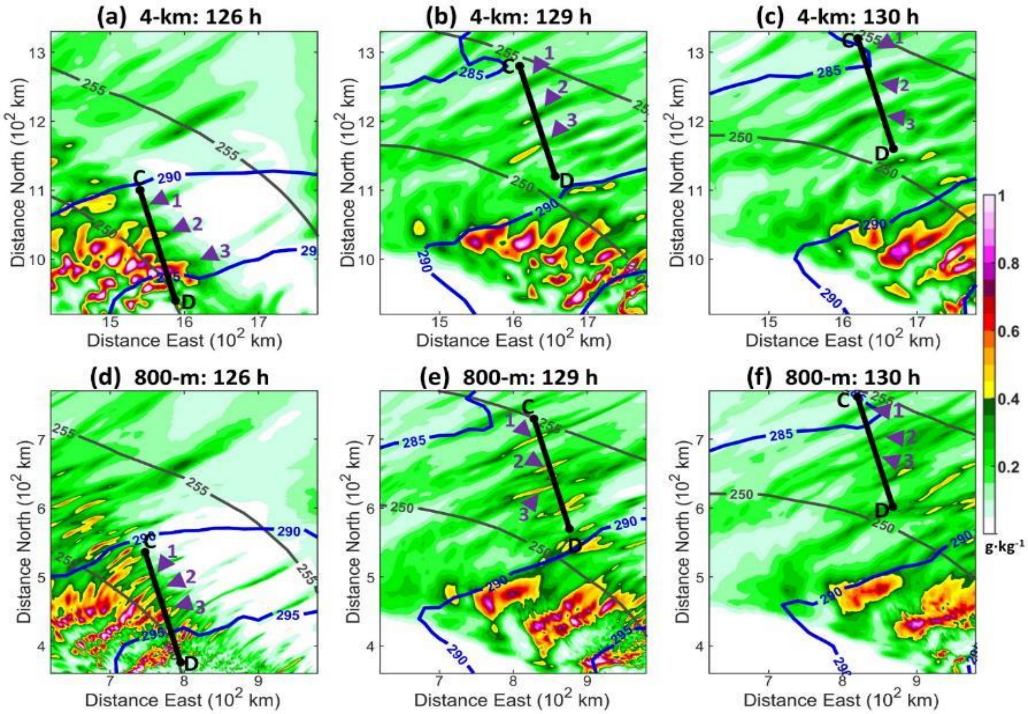

Figure 5: 700-hPa snow and ice mixing ratios (shaded), 700-hPa geopotential heights (black contours; every 5 dam), and 700-600-hPa potential temperature (blue contours; every 5 K) of the 4-km control run at (a) 126 h, (b) 129 h, and (c) 130 h. Each tick is 100 km. The locations of three developing bands are marked with purple arrows, numbered 1, 2, and 3. (d), (e), and (f), are the same as (a), (b), and (c), except for the 800-m. The black lines mark the locations of cross-sections taken from C to D and plotted in Figs. 6 and 7.

Cross-sections following the three bands (1, 2, and 3 in Fig. 5) help document their evolution in the 4-km and 800-m grids. At 126 h, the bands in the 4-km start as broad intense plumes (Fig. 6a). The 0.4-g·kg^{-1} contour in snow mixing ratios around band 3 reaches ~30 km in width. These plumes are separated from each other by 40-50 km. By comparison, in the 800-m, the same three plumes are narrower by 5-10 km and band 1 has twice as much snow above 650 hPa (Fig. 6d). The 800-m also separates the plumes by only 20-30 km and has more transient activity surrounding them.

By 129 h, the bands in the 4-km have matured (cf. Fig. 4b), at which point the 0.4-g·kg^{-1} snow contour of band 3 has narrowed to ~15 km in width (Fig. 6b). The largest snow mixing ratios (0.3-0.5 g·kg^{-1}) in the three bands are elevated between 650 and 500 hPa and correspond to vertical velocities of 0.2-0.3 m·s^{-1} in this layer. The separation between the 4-km bands is 30-40 km. The same three bands in the 800-m have now narrowed to less than 10 km in width (Fig. 6e). Band 1 in the 800-m still has 60% more snow than band 1 in the 4-km. Similar to the 4-km, the 800-m now separates the bands by 30-40 km and the largest snowfall and ascent in each plume are located around 650-500 hPa.

By 130 h, the snow and upward motion in both the 4-km (Fig. 6c) and 800-m (Fig. 6f) bands have decreased by 20-50%. The snow plumes in the two grids are comparable, separated by 30-50 km. Thus, the bands in the 4-km and 800-m grids become more comparable in spacing and length scale as they begin to elongate. The bands in both grids then decay in a similar manner. Given the similarities between the 4-km and 800-m bands, the rest of the paper will utilize the 4-km grid.

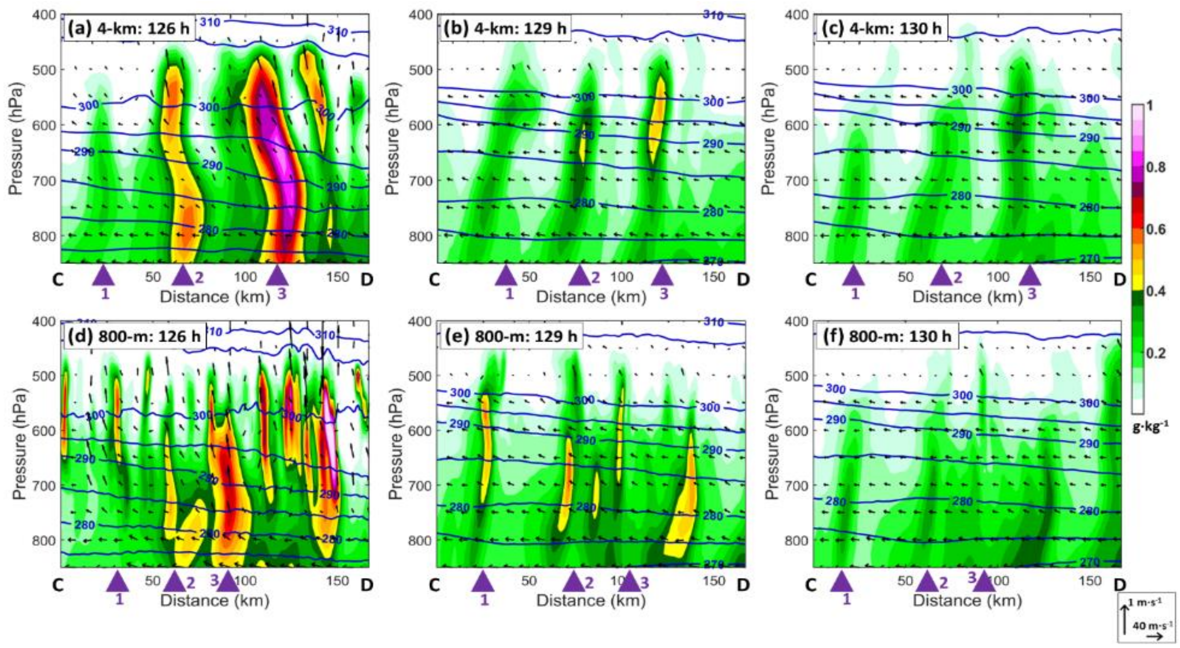

Figure 6: cross-sections of snow and ice mixing ratios (shaded), θ (blue contours; every 5 K), and circulation vectors of the 4-km at (a) 126 h, (b) 129 h, and (c) 130 h. The locations of the three bands tracked in Fig. 5 are marked by arrows. (d), (e), and (f), are the same as (a), (b), and (c), except for the 800-m.

The similar growth and decay of the bands in the 4-km and 800-m nests is likely due to similarities in the environments that the bands encounter as they advance further north of the low. The same C-D cross-section is used to examine the stability and 2D Pettersen (1936) frontogenesis. To minimize perturbations from the convection, only the 4-km is plotted, and a nine-point smoothing filter is applied to each vertical level of frontogenesis 20 times. The conditional (CI) and potential instabilities (PI) encountered by the bands are also assessed by contouring negative regions in the height-rate-of-change in saturated equivalent potential temperature ($d\theta_{es}/dz$) and equivalent potential temperature ($d\theta_e/dz$), respectively. Inertial and symmetric instabilities were also examined but found to be less significant (further discussion in Section 4).

At 126 h, band 3 is near a region of 5-7 K·(100 km)$^{-1}$·h^{-1} frontogenesis between 700 and 600 hPa (Fig. 7a). The frontogenesis slopes upwards to ~500 hPa near band 2 and weakens northward toward band 1. There are also regions of CI and PI between 650 and 500 hPa, sloping upwards from point D to C. By 129 h, the bands have moved away from the 700-600-hPa frontogenesis to the south, which is now less than 1 K·(100 km)$^{-1}$·h^{-1} near band 3 (Fig. 7b). Band 1 is approaching a thin weaker layer of ~3 K·(100 km)$^{-1}$·h^{-1} frontogenesis located near C above 600 hPa. The CI and PI near all three bands are now almost completely depleted. By 130 h, the bands have moved deeper into the 600-550-hPa frontogenesis near point C (Fig. 7c); however, all three bands quickly weaken regardless (Fig. 6). The 4-km captures many of the overall characteristics of these bands and their interaction with the environments they encounter.

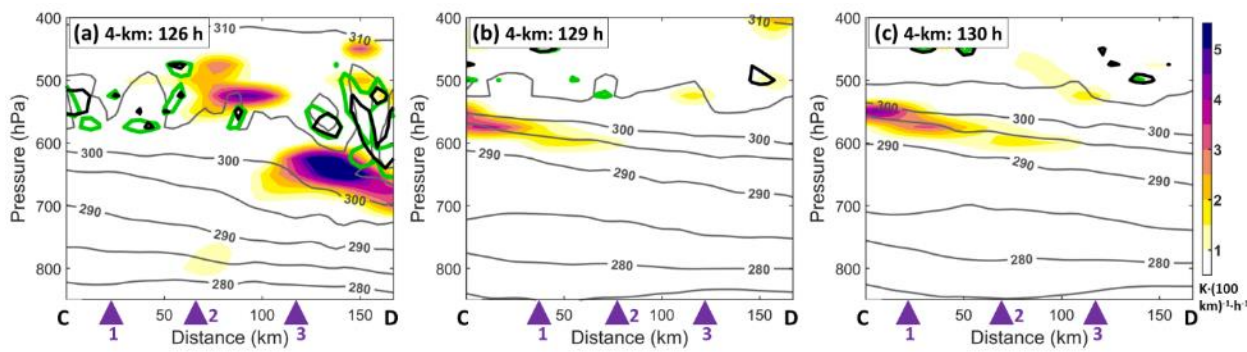

Figure 7: cross-sections of 2D Pettersen frontogenesis (shaded) and θ_e (grey contours; every 5 K) of the 4-km at (a) 126 h, (b) 129 h, and (c) 130 h. Regions where $d\theta_{es}/dz$ and $d\theta_e/dz$ are negative are contoured in black and green, respectively. The locations of the three bands tracked in Fig. 6 are marked by arrows.

The persistence of the bands after they move out of a region of instability and frontogenesis may be related in part to the time it takes for snow to fallout within the bands. To understand this fallout and the origin of the air entering the bands, trajectories are calculated in the 4-km. More specifically, five backwards hydrometeor trajectories are released at 700 hPa along band 1 while it was weakening and elongating at 130 h (e.g., the northernmost points in Fig. 8b). The trajectory calculation uses the mean fall speed weighted by the mixing ratios of the different types of precipitation. Prior to reaching band 1 between 128 and 129 h (Fig. 8a), the trajectories move north-northeast, maintaining the same elevation at ~400 hPa (Fig. 8c). The trajectories begin to fall as they encounter the snow mass at 129 h, curving westward while encountering easterly winds around the 700-hPa low (Figs. 8b,d). The alignment and spacing of the trajectories change little during this fallout period, suggesting that the precipitation organizes into a band aloft at 500-400 hPa and not while falling to 700 hPa. Overall, even after the upward motion has substantially weakened by 130 h, the snow that developed near the top of the band takes 1.5 hours to descend 300 hPa (~3.5 km).

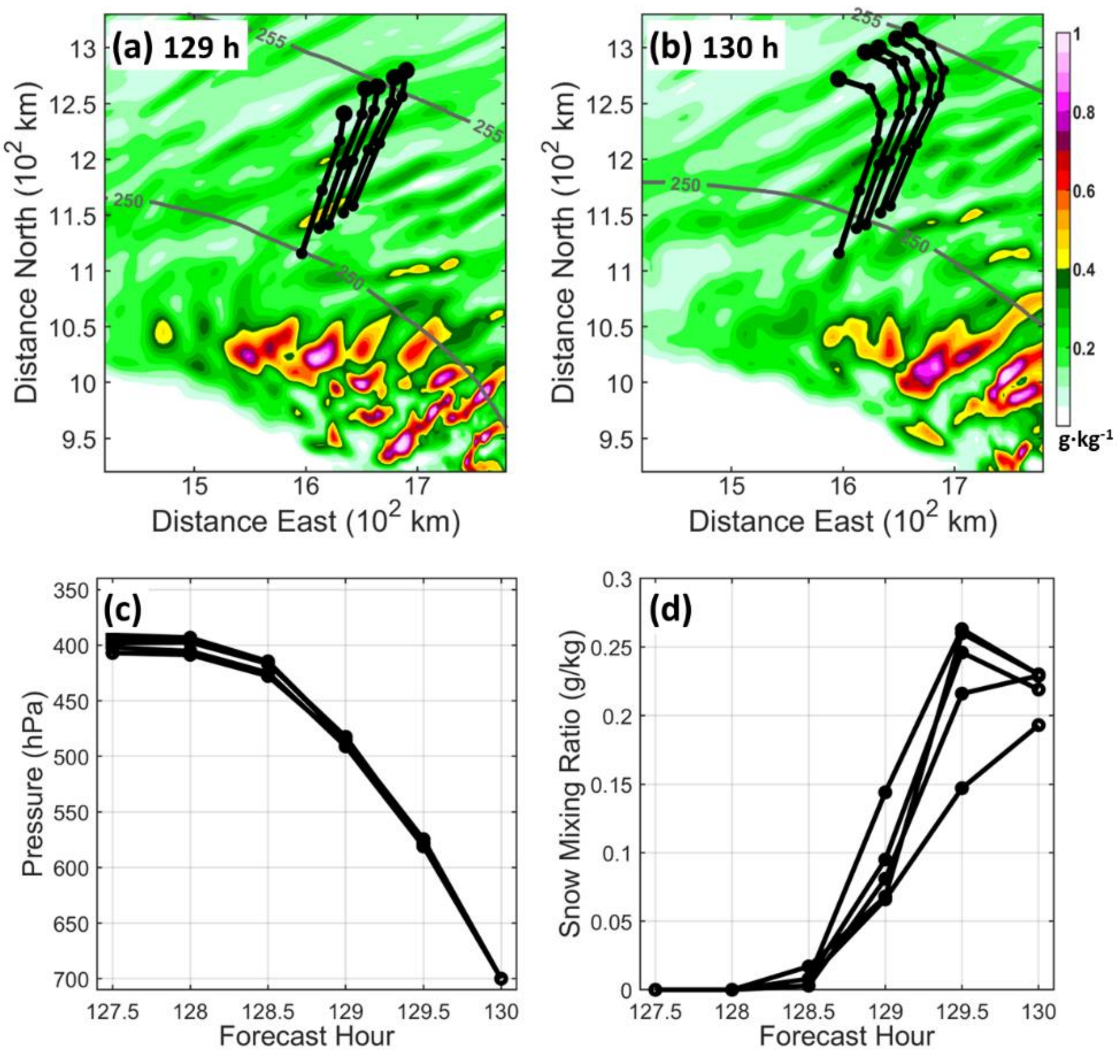

Figure 8: 700-hPa snow and ice mixing ratios (shaded every 0. 05 g kg^{-1}), 700-hPa geopotential heights (black contours; every 5 dam), and 700-hPa θ (blue contours; every 5 K) of the 4-km control run at (a) 129 h, and (b) 130 h. Each tick is 100 km. The five hydrometeor trajectories are marked with black lines, their positions every 30 minutes from 127.5 h marked by dots. (c) pressure and (d) snow mixing ratios of the trajectories with time.

4. Large-Scale Banding Environment

The stages of band activity (genesis, maturity, and decay) are put in the context of the larger scale synoptic features and ingredients (e.g., lift and stability). For this analysis, the 20-km grid is examined. The forcing for ascent is quantified using Q-vectors (Hoskins et al. 1978) and Pettersen frontogenesis. To remove small-scale variations, a nine-point smoothing filter is applied ten times to the temperature and height fields. The 700-500-hPa layer is analyzed for Q-vectors and 600-700-hPa for the frontogenesis, as these layers would favor the triggering of the precipitation bands. To put these results in context with the 4-km results, point C marks the middle point of the cross-sections in Fig. 3. At 111 h, there is 700-500-hPa Q-vector convergence along a boundary 200-400 km southeast of the 700-hPa low center and 100-200 km north of the low (Fig. 9a). In between these regions is 700-500-hPa upward motion over point C. The 700-600-hPa frontogenesis shows the most consistency with the eastern portion of this convection (Fig. 9g), albeit it is generally weak (<1 K$\cdot$(100 km)$^{-1}\cdot$h^{-1}). By the genesis phase at 120 h, the largest upward motion over the development region increases by 70%, and the adjacent Q-vector convergence increases by 20-40% (Fig. 9b). Meanwhile, the enhanced frontogenesis near point C now exceeds 2 K$\cdot$(100 km)$^{-1}\cdot$h^{-1}. By 138 h, the Q-vector convergence (Fig. 9c), frontogenesis (Fig. 9i), and upward motion decrease ~20%. Thus, the 700-500-hPa Q-vector convergence and frontogenesis peak around the genesis phase of the system and decrease afterwards.

The stages in band development are also put in context of the evolving vertical shear in the 600-500 hPa layer. At 111 h, the shear is 8-10 m$\cdot$s$^{-1}\cdot$km^{-1} in a southwesterly (band-parallel) direction within ~200 km north and west of point C (Fig. 9d). By 120 h, the southwesterly shear has increased up to 13 m$\cdot$s$^{-1}\cdot$km^{-1} over a band extending 200-400 km northwest of point C and a broader region from the east (Fig. 9e). At 138 h, the area of shear >11 m$\cdot$s$^{-1}\cdot$km^{-1} broadens, encompassing point C (Fig. 9f). Thus, southwesterly wind shear generally increases throughout the phases in banding activity.

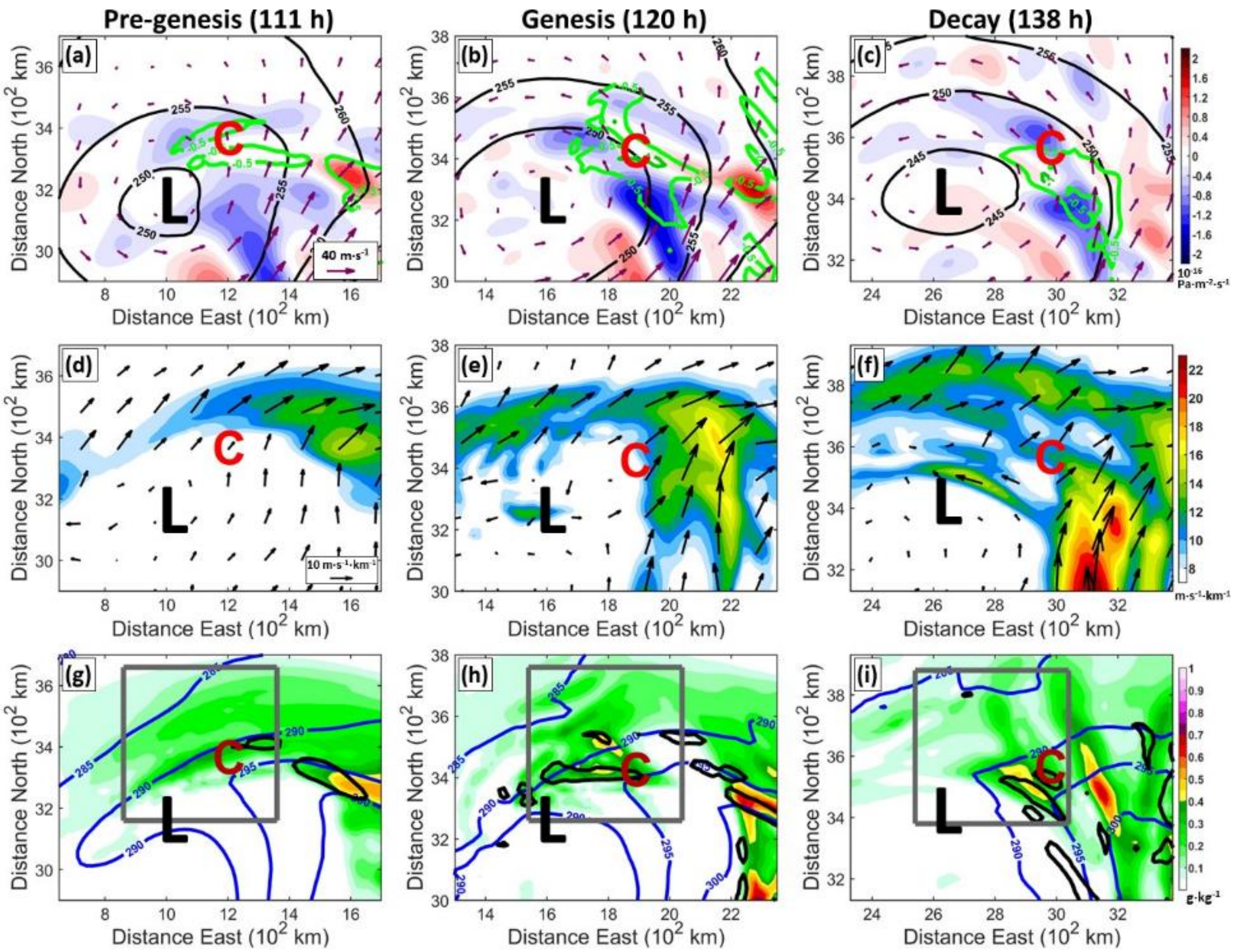

Figure 9: 700-500-hPa Q-vector divergence (shaded), 700-hPa geopotential heights (black contours; every 5 dam), 700-500-hPa wind vectors, and 700-500-hPa ω < 0 (green contours; every 0.5 $Pa \cdot s^{-1}$) of the 20-km control at (a) 111 h, (b) 120 h, and (c) 138 h. Each tick is 200 km. “C” marks the middle of the cross-sections in Fig 3. (d), (e), and (f), are the same as (a), (b), and (c), except showing 600-500-hPa vertical wind shear vectors and speed (shaded). (g), (h), and (i) are the same as (a), (b), and (c), except showing 700-hPa snow and ice mixing ratios (shaded), 700-600-hPa potential temperature (blue contours; every 5 K), 700-600-hPa frontogenesis >1 $K \cdot (100\ km)^{-1} \cdot h^{-1}$ (black contours), and the box used to create the area-average timeseries in Fig. 10.

To better examine the relationship between the environmental changes and the stages of band development, several environmental variables are calculated within a 500-by-500-km box following cyclone in the region of the 20-km grid where the bands develop (e.g., the box in Fig. 10g-h). The box moves such that it captures the wedge of snowbands to the northwest of the 700-600-hPa TROWAL. The size of the box is a compromise that also captures the shear further northwest, and the forcing and instability from the south. For clarity, the results are only shown for the 700-600-hPa and 600-500-hPa layers. The box-averaged 700-600-hPa frontogenesis quickly increases at 117 h and reaches its maximum by 124-127 h before gradually decreasing (Fig. 10a). The vertical wind shear is largest at 600-500 hPa and almost doubles between 108 h and 130 h (Fig. 10b). Thus, the shear may be too weak to organize the convection into parallel bands prior to 120 h.

Given that box-averages result in cancellation between the negative and positive regions of $d\theta_e/dz$ and $d\theta_{es}/dz$, the minimum value anywhere within the box is used. The box-minimum in $d\theta_e/dz$ indicates that PI in both the 700-600-hPa and 600-500-hPa layers is largest in amplitude between 108 h and 118 h (Fig. 10c). During this period, the magnitude of CI in both layers is less than half that of PI. The 700-600-hPa CI is depleted (e.g., $d\theta_{es}/dz$ reaches zero) by 126 h. Meanwhile, CI in the 600-500-hPa layer and PI in both layers are not fully depleted by the decay phase, with $d\theta_{es}/dz$ and $d\theta_e/dz$ reaching -1 $K \cdot km^{-1}$ between 126 and 136 h. The 600-500-hPa PI decays slowest, only reaching -1 $K \cdot km^{-1}$ by 136 h. Thus, the amplitude of 600-500-hPa PI shows the most consistency with the stages in banding activity, growing largest shortly before the genesis stage and maintaining most of its amplitude through the mature stage as it slowly decays.

The areal coverages of CI and PI are given by the percentages of grid points inside the box where $d\theta_{es}/dz$ and $d\theta_e/dz$ are negative, respectively (Fig. 10d). CI and PI in both layers are most extensive around 112 h, though they are ~10% larger in the 600-500-hPa layer. In the 600-500-hPa layer, the area of PI between 112 h and 129 h is ~10% larger than that of CI. Thus, 600-500-hPa PI covers the largest area within the region where the bands develop.

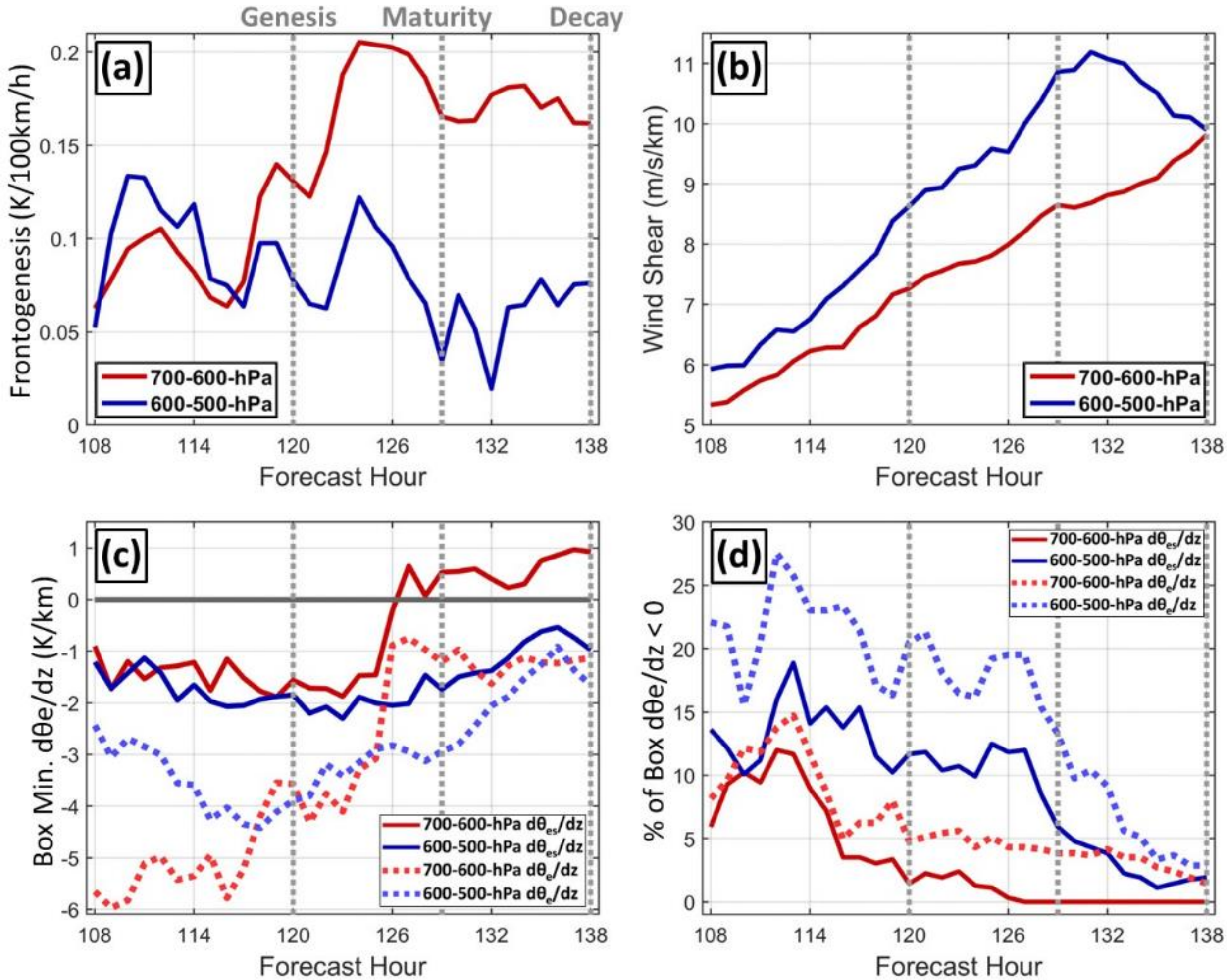

Figure 10: time series of statistics calculated within the moving box shown in Fig. 9. The statistics are calculated from the 20-km domain averaged over the layers indicated in the legend. (a) area-averaged frontogenesis, (b) area-averaged vertical wind shear, (c) box-minima in $d\theta_e/dz$ (dashed lines) and $d\theta_{es}/dz$ (solid lines), and (d) the percentage of the box in which $d\theta_e/dz$ (dashed lines) and $d\theta_{es}/dz$ (solid lines) are negative.

The development of the instabilities is further analyzed in Figure 11, which shows the locations of CI, CSI, PI, and PSI relative to the developing baroclinic wave at three different times. The 600-550-hPa layer is used since this is where the instabilities are largest in the band cross-sections (e.g., Fig. 7). Inertial instability was also analyzed but was not present anywhere near the banding activity (not shown).

At 111 h, $d\theta_{es}/dz$ is between -0.5 and -1.5 $K \cdot km^{-1}$ at ~400 km west and ~100 km north of point C (Fig. 11a). CI is also present at 700-650 hPa over a narrow band south of point C, where the cells develop in the wedge (not shown). Given the large overlap between CI and negative saturated moist potential vorticity (MPV*) around point C, much of this convective activity is not from CSI. By the genesis phase at 120 h, the negative $d\theta_{es}/dz$ at 600-550-hPa grew from -1.5 to -2.0 K·km^{-1} extending 100-200 km north and west of point C (Fig. 11b). CSI only exists (negative MPV* but no CI) to the southeast of point C. During the decay phase at 138 h, the CI has been depleted, leaving only a small region 50-100 km southeast of point C where $d\theta_{es}/dz$ is -1.5 K·km^{-1} (Fig. 11c).

Surrounding this CI is a region of PI in the 600-550-hPa layer. The negative values in $d\theta_e/dz$ range from -2.0 K·km^{-1} at 111 h (Fig. 11d), to -3.5 K·km^{-1} at 120 h (Fig. 11e), to -2.5 K·km^{-1} at 138 h (Fig. 11f). Thus, 600-550-hPa CI and PI are the dominant instabilities where the bands develop northeast of the low, both of which increase leading up to the genesis phase and are depleted approaching the decay phase. The cells first develop within 700-600-hPa CI at the southern tip of the wedge and grow into bands as they move northward into 600-500-hPa PI.

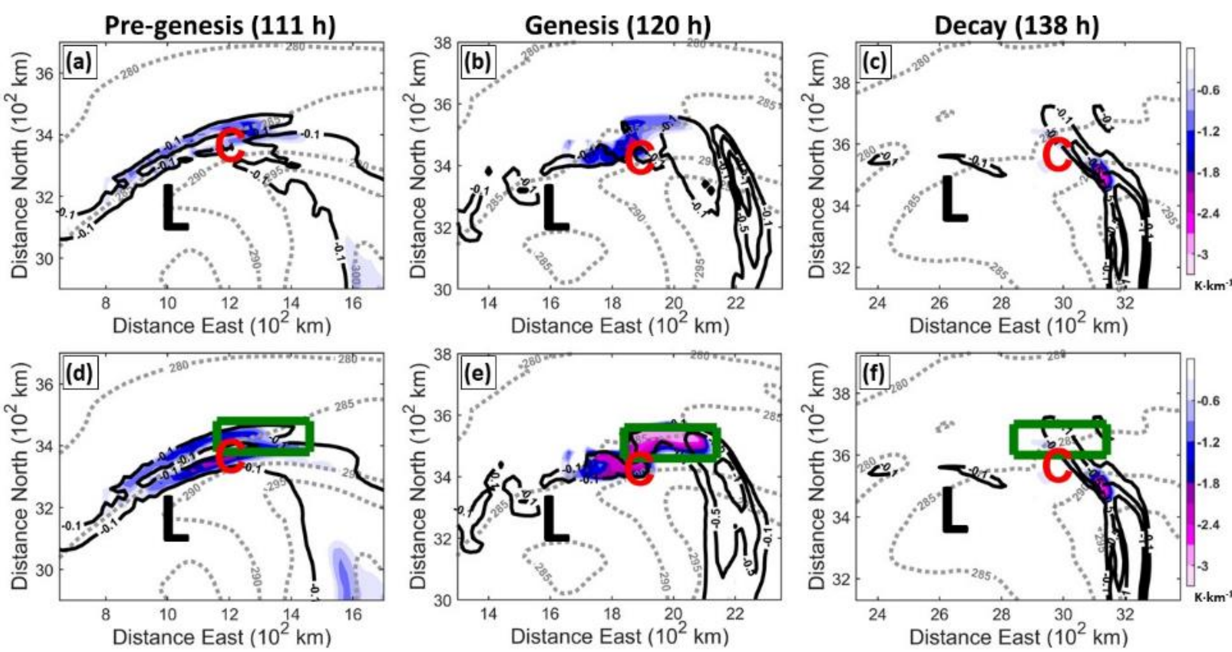

Figure 11: 600-550-hPa $d\theta_{es}/dz < 0$ (shaded) and MPV* < 0 (black contours; PVU), and 700-hPa potential temperature (grey dash; every 5 K) of the 20-km control at (a) 111 h, (b) 120 h, and (c) 138 h. Each tick is 200 km. "C" and "L" mark the middle point of the cross-sections and the surface low center positions in Fig 3, respectively. 600-550-hPa $d\theta_e/dz < 0$ (shaded) and MPV < 0 (contours; PVU), and 700-hPa potential temperature (green contours; every 5 K) of the 20-km control at (d) 111 h, (e) 120 h, and (f) 138 h. The green box is where area-averages are calculated to create the vertical profiles in Fig. 12.

The source of the 600-500-hPa PI before the genesis phase is examined with vertical profiles averaged over a box (300 km west-to-east and 100 km south-to-north) targeting the PI that grew north of point C by 120 h (e.g., Fig. 11e). This same region relative to point C is traced back to 111 h for comparison, at which point there was only half as much PI (Fig. 11d). The subsequent decrease in PI is also investigated by following the boxed region north of point C to 138 h (Fig. 11f). The profiles of saturated equivalent potential temperature (θ_{es}) and equivalent potential temperature (θ_e) at 111 h both decrease by ~1 K between 550 and 475 hPa, confirming that there is CI and PI within this layer (Fig 12a). By 120 h, the θ_e profile becomes steeper, decreasing by 2 K between 575 and 500 hPa (Fig. 12b). Meanwhile, the dry θ profile becomes slightly more stable within the 550-500-hPa layer, such that most of the change in θ_e comes from changes moisture. At 138 h, the layer of PI is elevated, though θ_e only decreases by 0.7 K between 525 and 450 hPa (Fig. 12c).

The increase in PI between 111 h and 120 h is consistent with differential θ_e advection in the vertical. More specifically, θ_e advection within the box at 111 h switches from positive at ~600 hPa to negative at ~550 hPa (Fig. 12d). At 120 h, the negative advection at ~550 hPa increases by ~70%, such that the differential θ_e advection increases, resulting in a steeper more unstable θ_e profile in the 600-550-hPa layer (Fig. 12e). While the 550-hPa dry θ advection also becomes more negative, it is around half as large as the θ_e advection, suggesting the importance of moisture advection. At 138 h, the negative θ_e advection weakens by ~70% and elevates above 500 hPa, consistent with the differential θ_e advection decreasing and a less unstable θ_e profile in the 600-500-hPa layer (Fig. 12f).

The importance of moisture in the changes in PI is analyzed within the same box. The profile of specific humidity advection at 111 h is consistent with the θ_e advection, switching from positive at ~600 hPa to negative (dry) at ~550 hPa (Fig. 12g). At 120 h, the dry advection at ~550 hPa doubles in magnitude, consistent with the increase in differential θ_e advection (Fig. 12h). At 138 h, the dry advection is halved and elevates above 500 hPa, consistent with the θ_e advection (Fig. 12i).

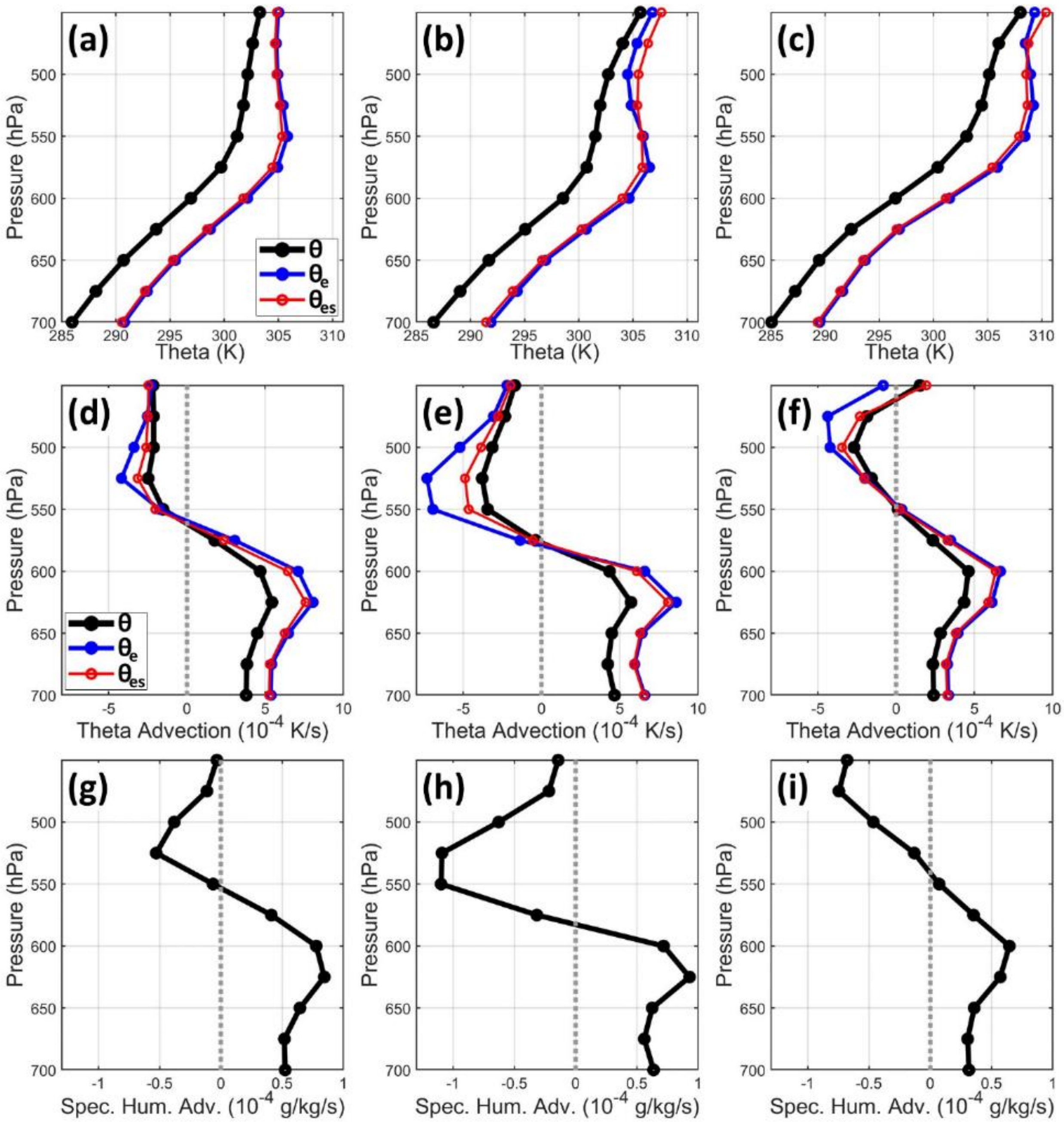

Figure 12: Box-average profiles of potential temperature, equivalent potential temperature, and saturated equivalent potential temperature at (a) 111 h, (b) 120 h, and (c) 138 h. Box-average profiles of advection of potential temperature, equivalent potential temperature, and saturated equivalent potential temperature at (d) 111 h, (e) 120 h, and (f) 138 h. Box-average profiles of specific humidity advection at (g) 111 h, (h) 120 h, and (i) 138 h.

5. Band Sensitivity to Changes in Environmental Parameters

a. *Approach*

Additional experiments test the sensitivity to small changes in the initial conditions, adjusting environmental parameters that are expected to affect snow band development. In one experiment, the initial dry stability is effectively increased by ~10% throughout the domain (hereafter called "STAB+10"). More specifically, the potential temperature (θ) profile at each grid point is adjusted by a linear function, such that the top (bottom) model level is 8.5 K warmer (cooler) than the original control run. As a result, the height-rate-of-change in potential temperature (dθ/dz) is increased by ~1 $K \cdot km^{-1}$ everywhere. Note that, in each of these experiments, the mass and wind fields are adjusted to maintain hydrostatic and geostrophic balance. Thus, when the initial STAB+10's jet winds are ~4 $m \cdot s^{-1}$ faster than the control run above the break in the tropopause (Fig 13b). For the second experiment (STAB+5), the initial stability is increased by only 5% across the domain. Experiments in which the stability is reduced by 5-10% become numerically unstable before 108 h and are therefore not included.

The last experiment (TGRAD-10) tests the effects of reducing the initial horizontal θ gradient by 10%. This is achieved by first finding the domain-average θ at each vertical level. Then, the anomaly with respect to that average θ is calculated at each grid point. These anomalies are then multiplied by 0.9, thus reducing their departure from the domain-average by ~10%. As a result, the 1000-400-hPa θ is reduced (increased) on the warm southern (cool northern) side of the jet (Fig 13c). The reduced θ gradient corresponds to the 300-hPa jet weakening by ~6 $m \cdot s^{-1}$. The effects of reducing the θ gradient by 5% (TGRAD-5) and increasing the θ gradient by 5% (TGRAD+5) and 10% (TGRAD+10) are also tested. In each of these experiments, the 1000-700-hPa temperatures remain at least 10 K below freezing where the bands develop northeast of the low, such that the precipitation is largely snow.

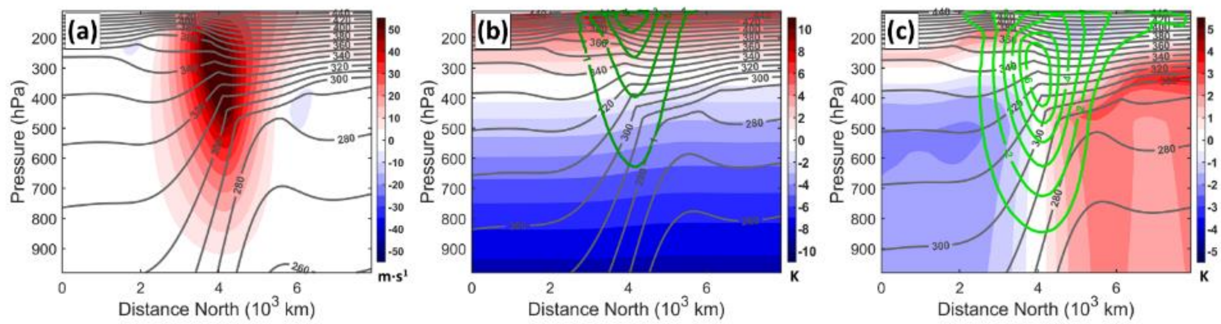

Figure 13: (a) U-wind (shaded; every 5 m·s^{-1}), and potential temperature (contours; every 5 K) of the initial input jet data used for the control run. (b) Initial STAB+10 – control run differences in θ (shaded) and U-wind (dark green contours > 0, light green contours < 0; m·s^{-1}), and STAB+10 θ (grey contours; every 5 K). (c) Initial TGRAD-10 – control run differences in θ (shaded) and U-wind (dark green contours > 0, light green contours < 0; m·s^{-1}), and TGRAD-10 θ (grey contours; every 5 K).

Adjusting the thermal stability and horizontal temperature gradient of the initial conditions also affects the development of the large-scale baroclinic wave. The sea-level pressure minimum in the 100-km grid is associated with the developing low pressure center (Fig. 14). The runs in which either the initial stability is increased or the horizontal temperature gradient is decreased delay the development of the low by ~12 h. Changing the horizontal θ gradient affects the intensity of the jet and hence the forward speed of the surface low (not shown). As the analysis moves with the low center, the locations compared within the domain will differ between runs.

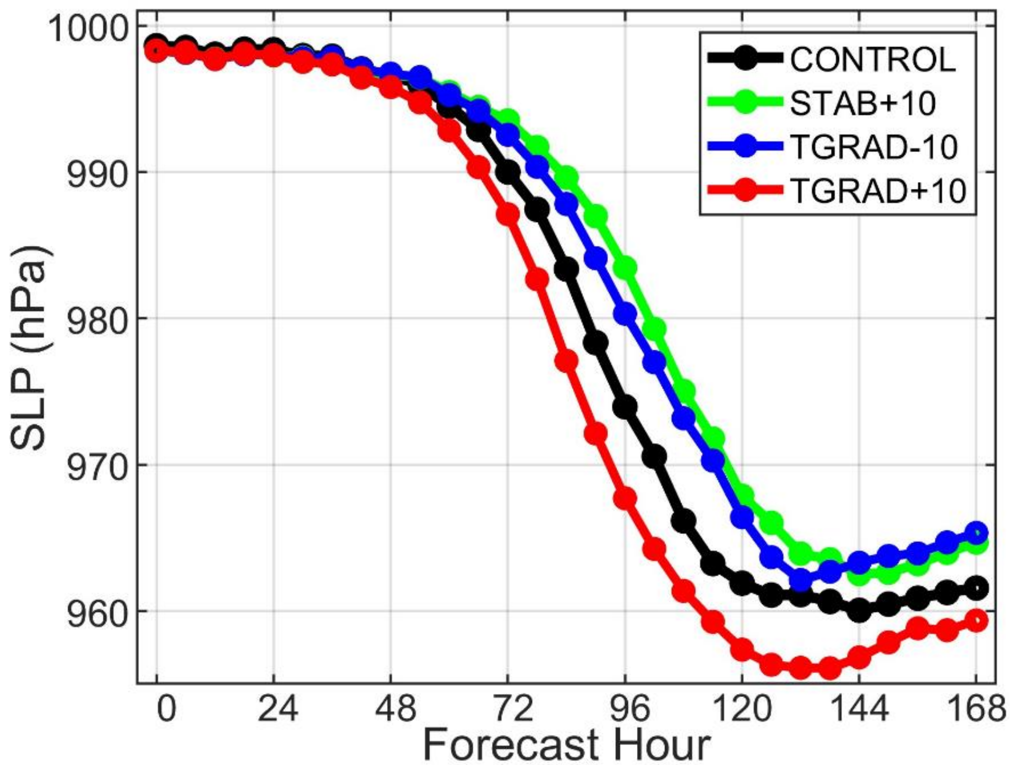

Figure 14: time series of the grid-point-minimum sea-level pressure within the 100-km control (black line), STAB+10 (green line), TGRAD+10 (red line), and TGRAD-10 (blue line) runs.

b. Results

The convective activity around the developing system is compared between the 4-km runs in which the initial stability is increased. Differences in the extent of convection develop at 120 h (the genesis phase of the control run). The STAB+5 run spins-up a region of cellular convection that resembles a wedge 100-300 km east-northeast of the surface low and west of the 290-K isentrope protruding along the 700-hPa TROWAL (Fig 15a). At 129 h (the mature phase of the control run), the STAB+5 run further organizes the convection northeast of the low into a wedge more closely resembling the control run, forming small (<100 km long) bands oriented southwest-to-northeast (Fig. 15b). At 138 h (the decay phase of the control run), the STAB+5 run shows an increase in bands oriented southwest-to-northeast (Fig. 15c). This banding activity persists for four hours (not shown), compared to the 18-hour duration in the control run.

By comparison, the STAB+10 run has a less organized region of cellular activity east of the low at 120 h (Fig. 15d). At 129 h, the STAB+10 run develops a narrow wedge of convection

100-200 km east-northeast of the low (Fig. 15e). The snow mixing ratios within this wedge are less than half that of the STAB+5 run. East along the TROWAL, four 200-km-long bands are oriented northwest-to-southeast, parallel to the 800-700-hPa vertical wind shear. These bands dissipate within the subsequent three hours (not shown). At 138 h, any band activity in the STAB+10 run has disappeared (Fig 15f). Thus, there is an overall decrease in banding activity during the mature stage with increased initial stability. However, increasing the stability by only five percent results in bands developing nine hours later than the control run.

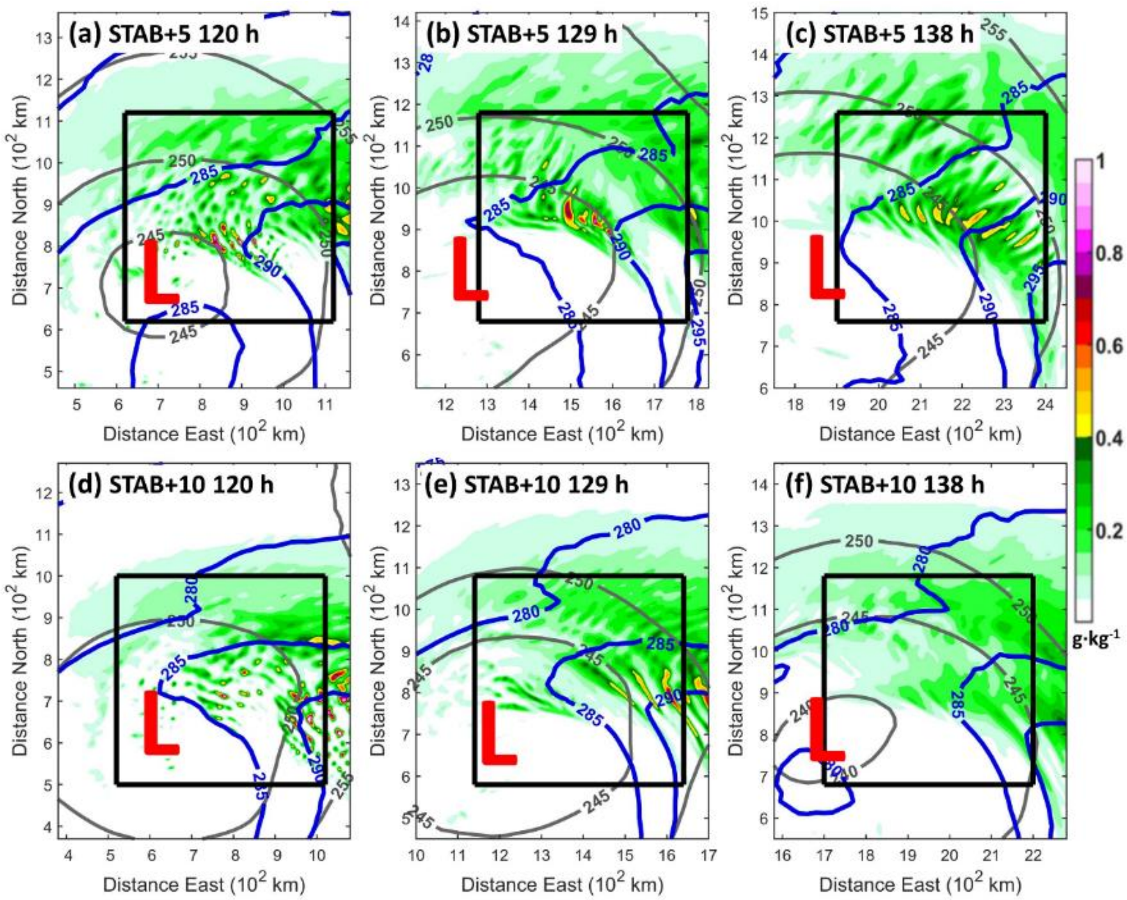

Figure 15: 700-hPa snow and ice mixing ratios (shaded), 700-hPa geopotential heights (black contours; every 5 dam), and 700-600-hPa potential temperature (blue contours; every 5 K) of the 4-km STAB+5 run at (a) 120 h, (b) 129 h, and (c) 138 h. The position of the surface low pressure center is marked by an L, and the box is where area-averages are taken in the 20-km grid to create the time series in Fig. 16. (d), (e), and (f) are the same as (a), (b), and (c), except for the 4-km STAB+10 run.

The evolution of the environments in these runs are compared by averaging variables within a moving 500-by-500-km box in the 20-km grid. As with the control run in Fig. 10, the box in each run encompasses the wedge of snowbands east of the surface low and west of the 700-600-hPa TROWAL, following the system as it advances eastward. The 600-500-hPa vertical velocity in the control run reaches its peak between 118 and 127 h and is ~1 $cm{\cdot}s^{-1}$ (~20%) greater than both the STAB+5 and STAB+10 runs (Fig. 16a). However, while the control run upward motion weakens after 127 h, the STAB+5 run continues to slowly increase. The weaker upward motion in the STAB+5 and STAB+10 runs is consistent with these runs also having 25-50% weaker 700-600-hPa frontogenesis after 120 h, though the STAB+5 frontogenesis decreases after 126 h (Fig. 16b).

The less organized convection in the STAB+5 and STAB+10 runs may also correspond to weaker vertical wind shear. By the genesis phase at 120 h, the 600-500-hPa wind shear of the control run is up to 10% (40%) greater than the STAB+5 (STAB+10) run (Fig. 16c). However, after 131 h, the control run wind shear starts to decrease, while the STAB+5 run increases to the same magnitude as the control run by ~138 h. Thus, increases in initial stability also correspond to decreases in wind shear during much of the genesis phase, resulting in less banding activity northeast of the low.

Given the initial moisture of the model is prescribed by a relative humidity profile, cooling the lower model levels to increase the stability also reduces the total moisture content. The differences in precipitable water between the runs are generally consistent throughout time, with the STAB+5 and STAB+10 runs having ~1.0 mm (~20%) and ~2.0 mm (~35%) less moisture than the control run, respectively. This reduction in moisture may also contribute to the weaker snowfall in general.

Prior to 108 h, the differences in PI around the low between the STAB+10 and control runs grow well above 10%, corresponding to changes in differential temperature and moisture advection (not shown). In Fig. 16d, the amplitude of PI is estimated by the box-minimum in 600-500-hPa $d\theta_e/dz$. Between 114 h and 120 h, the magnitudes of PI in the STAB+5 and STAB+10 runs are 2 $K{\cdot}km^{-1}$ (~50%) and 3 $K{\cdot}km^{-1}$ (~80%) less than the control run, respectively. However, between 118 h and 132 h, the magnitude of PI in the control run decreases by 2.5 $K{\cdot}km^{-1}$ (~50%), while the STAB+5 run becomes 1.0 $K{\cdot}km^{-1}$ larger than the control. After 132 h, the STAB+5 run maintains PI close to -3 $K{\cdot}km^{-1}$.

The area coverage of 600-550-hPa PI within the box is compared in Fig. 16f. Between 108 h and 132 h, the regions of PI in the STAB+5 and control runs are of similar size, while the

STAB+10 run is up to 15% smaller than the control run until 117 h. Then, between 133 h and 138 h, the area of PI in the STAB+5 run is up to 7% larger than the STAB+10 and control runs.

Thus, the amplitude of PI in the runs with increased initial stability is 50-80% less than that of the control run by 120 h, corresponding to overall less convection and banding activity. However, the STAB+5 maintains more PI than the control run during the six hours prior to the decay phase, long enough for the vertical wind shear to increase to values more comparable to the control. As a result, the STAB+5 run briefly develops multi-bands later during the decay phase of the control run.

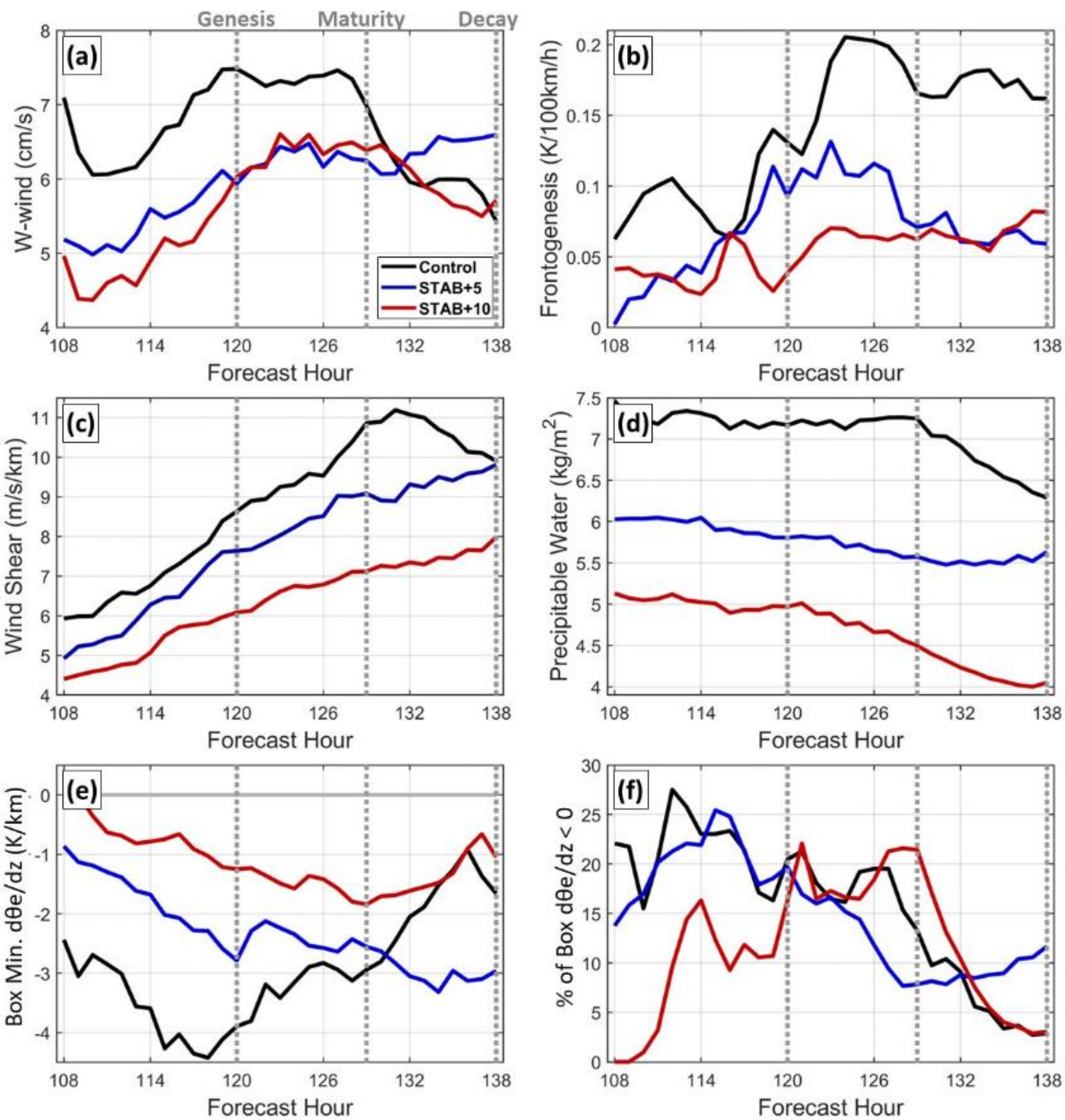

Figure 16: time series of statistics calculated within the moving boxes following the band development region in the 20-km domains of the control, STAB+5, and STAB+10 runs. Area-averaged (a) 600-500-hPa w-wind,

(b) 700-600-hPa frontogenesis, (c) 600-500-hPa vertical wind shear, and (d) precipitable water, and (e) box-minimum 600-500-hPa $d\theta_e/dz$, and (f) the percentage of the box in which 600-500-hPa $d\theta_e/dz$ is negative.

The effects of changing the initial horizontal temperature gradient are examined by comparing the 4-km precipitation (Fig. 17). Only the TGRAD+10 and TGRAD-10 runs are shown during times corresponding to the genesis, mature, and decay phases of the control run. Changing the gradient by only 5% results in precipitation patterns resembling a combination of the control run and the runs changed by 10% (not shown). Between 0 and 120 h, the 700-600-hPa temperature gradient along the northern edge of the TROWAL ~400 km east-northeast of the low in the TGRAD+10 run amplifies (Fig 17d), becoming ~30% greater than the control run. Meanwhile, the TGRAD-10 run temperature gradient along the northern edge of the TROWAL is ~15% less than the control run at 120 h (Fig 17a).

The TGRAD-10 run is still developing disorganized cellular convection within 300 km east and north of the low at 120 h (Fig. 17a), whereas the control run at this time organized the convection into a wedge shape. By 129 h, the TGRAD-10 run starts to develop cellular convection 200-400 km east of the low and along the 295-K isentrope of the TROWAL (Fig. 17b). This convection forms small (~100-km long) SW-NE segments by 138 h (Fig. 17c), though they quickly dissipate as they propagate northward around the low (not shown).

The TGRAD+10 4-km run develops multiple SW-NE-oriented bands within a large wedge east and north of the low by 120 h (Fig. 17d), already resembling the mature phase of the control run (c.f. Fig. 3c). Between 129 h (Fig. 17e) and 138 h (Fig. 17f), the southern portion of the wedge between the 290-K and 295-K isentropes along the TROWAL collapses into a single NW-SE band. However, there are still SW-NE bands being generated more than 200 km north of low. Thus, decreasing the temperature gradient by 10% delays the organization of convection east of the low by nine hours and reduces the northward extent of the banding activity. Conversely, increasing the temperature gradient promotes more banding activity that reaches its peak nine hours earlier than the control run.

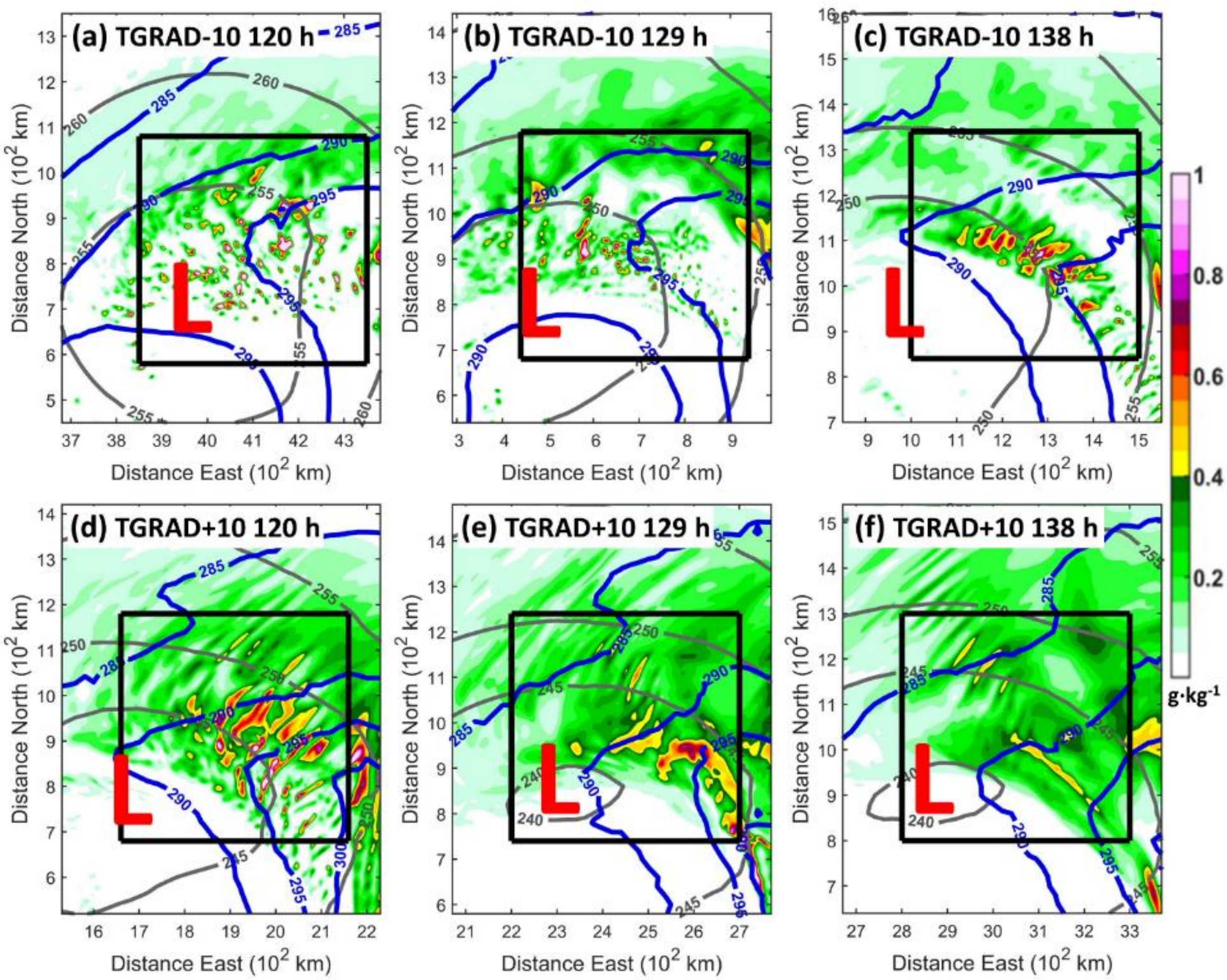

Figure 17: 700-hPa snow and ice mixing ratios (shaded), 700-hPa geopotential heights (black contour; every 5 dam), and 700-600-hPa potential temperature (blue contour; every 5 K) of the 4-km TGRAD-10 run at (a) 120 h, (b) 129 h, and (c) 138 h. The position of the surface low pressure center is marked by an L and the box is where area-averages are taken to create the time series in Fig. 18. (d), (e), and (f) are the same as (a), (b), and (c), except for the TGRAD+10 run.

The evolution of the environments in the 20-km grids are again compared taking averages within a moving 500-by-500-km box encompassing the wedge of multi-bands east of the low. The 700-600-hPa frontogenesis of the TGRAD+10 run grows ~40% larger than the control run by ~121 h (Fig. 18a). Afterwards, the TGRAD+10 frontogenesis decreases to ~30% of the control run by 128 h, and then increases back to the same magnitude as the control run by 137 h. This reduction in frontogenesis corresponds to evaporative cooling from the intense episode of precipitation reducing the temperature gradient (not shown). Meanwhile, the TGRAD-10 run frontogenesis generally increases over time, exceeding the control by 131 h.

The 600-500-hPa wind shear of the TGRAD+10 run between 114 h and 138 h is on average ~30% larger than the control run and ~60% larger than the TGRAD-10 run (Fig. 18b). Between 131 and 138 h, the wind shear of the control run decreases, while the TGRAD-10 run continues to increase, such that the difference between the two runs is less than 10% by 138 h. The larger frontogenesis at ~122 h in the TGRAD+10 run corresponds to more convective activity east of the low, while the larger shear corresponds to the convection organizing into longer bands.

The amplitude of PI is again estimated from the minimum in 600-500-hPa $d\theta_e/dz$ anywhere within the box (Fig. 18c). The PI in the TGRAD+10 run is close to that of the control between 108 h and 120 h. Afterwards, the TGRAD+10 PI decreases more slowly than the control, remaining below -3.5 K/km until 131 h, which is ten hours later than the control. Meanwhile, PI in the TGRAD-10 run increases between 116 h and 129 h, 20-50% greater than the control after 123 h.

The percentage of the box where there is PI in each run is plotted in Fig. 18d. PI in the TGRAD+10 run covers a region ~5% larger than the control between 115 h and 120 h. Afterwards, the region of PI in the TGRAD+10 run becomes smaller than the control, falling below 10% by ~123 h. While the PI in the TGRAD-10 run is overall weakest in amplitude, it covers a region that is 10-20% broader than the control after 114 h.

The faster maturity of banding activity in the TGRAD+10 run by 120 h is consistent with wind shear that is stronger than the control run throughout the simulation, a prior increase in frontogenesis, and PI comparable to the control run. The persistence of the banding activity in the TGRAD+10 run out to 138 h corresponds to the PI lasting longer than the control. Meanwhile, the delayed development of PI in the TGRAD-10 run corresponds to the band activity developing later, as the wind shear and frontogenesis increase to values comparable to the control by 138 h.

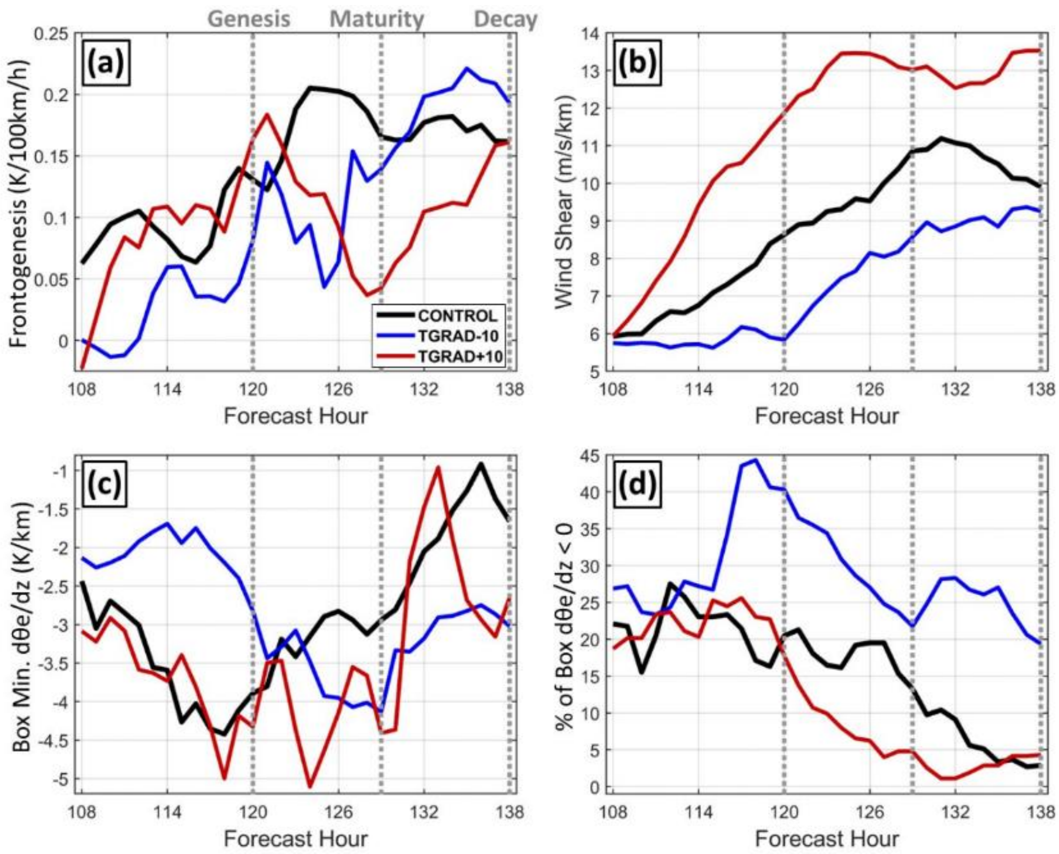

Figure 18: time series of statistics calculated within the moving boxes following the band development region in the 20-km domains of the control, TGRAD-10, and TGRAD+10 runs. Area-averaged (a) 700-600-hPa frontogenesis, (b) 600-500-hPa vertical wind shear, and (c) box-minimum 600-500-hPa $d\theta_e/dz$, and (d) the percentage of the box in which 600-500-hPa $d\theta_e/dz$ is negative.

6. Conclusions

The goal of this study is to better understand the environmental conditions under which snow multi-bands develop in the comma head of winter storms. The structure and evolution of snow bands are examined using the idealized baroclinic wave setup within the WRF model, which is nested down to 4-km and 800-m grid spacing. The 4-km bands are similar to the 800-m bands, so 4-km is used for much of the analysis, while the 20-km grid is used for the environmental conditions.

The idealized WRF model develops a wedge of snow multi-bands east of the maturing surface low and along a 700-600-hPa TROWAL at 120-138 h. The individual bands start as cells at the tip of the wedge and elongate into southwest-to-northeast bands as they propagate northward. Backwards hydrometeor trajectories taken within a mature band indicate that the snow first develops along the band at 500-400 hPa and does not elongate much further as it falls below 700 hPa. That is, the precipitation was already organized within a banded structure when it formed aloft. This differs from the generating cell mechanism in which fallout from cells aloft organizes into bands as it falls through a layer of shear or deformation.

PI and CI within the 700-500-hPa layer are the dominant instabilities where the bands develop. More specifically, there is 700-600-hPa CI where the cells first develop and 600-500-hPa PI extending north where the cells grow into bands. The PI is larger in amplitude, with $d\theta_e/dz < -3.0\ K \cdot km^{-1}$, and decays northward where the bands gradually diminish in amplitude. The appearance of the bands at ~120 h coincides with a growth in PI and CI from differential moisture advection, which corresponds to a dry intrusion wrapping around the low pressure system above 550 hPa. The activity dissipates 18 hours later after the differential advection weakens and the instability is depleted by the convection. Frontogenesis within the 700-600-hPa layer sharply increases up to the peak in banding activity at ~129 h and then gradually decreases as the banding activity subsides. The largest frontogenesis is located where the cells first develop and decays northward where the cells grow. The bands are oriented parallel to the 600-500-hPa vertical wind shear, which extends north of the maximum frontogenesis and increases from 6 $m \cdot s^{-1} \cdot km^{-1}$ at 108 h to 9-11 $m \cdot s^{-1} \cdot km^{-1}$ at 120 h.

Much like in case studies with multi-bands, the limited 18-hour time window over which the banding activity occurs in the simulation suggests a predictability challenge. Additional idealized experiments are conducted in which the stability profile and horizontal temperature gradient of the initial baroclinic wave are adjusted by 5-10% across the domain. The initial changes in stability grow such that the 600-500-hPa PI over the band development region in these runs is 50-80% less than the original control run by 114 h. Meanwhile, the 5-10% changes in the horizontal temperature gradient grow to 15-30% over the band development region by 120 h. Thus, the idealized baroclinic wave simulation is sensitive to small differences in the initial conditions, which greatly impact the environmental parameters affecting the snow bands.

Increasing the initial stability by 10% fully suppresses the development of multi-bands throughout the simulation, while increasing it by 5% only delays the development of multi-bands by 18 hours, at which point the PI and wind shear have increased to magnitudes comparable to the control run at 120 h. Meanwhile, decreasing the initial horizontal temperature gradient by 10% delays the growth of vertical shear and instability, corresponding to multi-bands developing 12-18 hours later. Conversely, increasing the horizontal temperature gradient by 10% corresponds to greater vertical shear earlier in the run, resulting in more prolific multi-band activity developing ~12 hours earlier. Thus, the 18-hour window in banding activity largely depends on the peak development of PI coinciding with the growth in shear.

Future work will address remaining questions. The individual bands persist for more than two hours despite moving into a region of weaker frontogenesis and PI over 500 km north of the low. Thus, what mechanisms are maintaining the bands? The bands grow parallel to the southwesterly 600-500-hPa shear. Does ambient shear play a role in this organization?

Acknowledgements: This work was funded by the National Science Foundation (AGS-1904809) and NASA IMPACTS (80NSSC19K0394).

Data Availability Statement: The full model output from the WRF simulations is too large to be publicly archived; each time step from the 4-km (800-m) grid is 3 GB (12 GB) in size. The precipitation and state variables for the times and subsets of the domain shown in this paper are archived in Stony Brook University's Google Drive https://drive.google.com/drive/folders/14fbRYcAq14e0mxQ0U3eIxjqP04UIrCm6?usp=drive_link

References:

Baxter, M., and P. Schumacher, 2017: Distribution of Single-Banded Snowfall in Central U.S. Cyclones. *Wea. Forecasting*, **32**, 533–554. DOI:10.1175/WAF-D-16-0154.1.

Connelly, R., and B. A. Colle, 2019: Validation of Snow Multibands in the Comma Head of an Extratropical Cyclone Using a 40-Member Ensemble. *Wea. Forecasting*, **34**, 1343–1363. DOI:10.1175/WAF-D-18-0182.1

Dowell, D. C., C. R. Alexander, E. P. James, S. S. Weygandt, S. G. Benjamin, G. S. Manikin, B. T. Blake, J. M. Brown, J. B. Olson, M. Hu, T. G. Smirnova, T. Ladwig, J. S. Kenyon, R. Ahmadov, D. D. Turner, J. D. Duda, and T. I. Alcott, 2022. The High-Resolution Rapid Refresh (HRRR): An Hourly Updating Convection-Allowing Forecast Model. Part I: Motivation and System Description. *Wea. Forecasting*, **37**, 1371–1395. DOI:10.1175/WAF-D-21-0151.1.

Evans, A. G., J. D. Locatelli, M. T. Stoelinga, and P. V. Hobbs, 2005: The IMPROVE-1 Storm of 1-2 February 2001. Part II: Cloud Structures and the Growth of Precipitation. *J. Atmos. Sci*., **62**, 3456–3473. DOI:10.1175/JAS3547.1.

Galloway, J. L., 1958: The Three-Front Model: It's Philosophy, Nature, Construction and Use. *Weather*, **13**, 293–301.

——, 1960: The Three-Front Model, the Developing Depression and the Occluding Process. *Weather*, **15**, 293–301.

Ganetis, S. A., B. A. Colle, S. E. Yuter, and N. P. Hoban, 2018: Environmental Conditions Associated with Observed Snowband Structures Within Northeast U.S. Winter Storms. *Mon. Wea. Rev*., **146**, 3675–3690. DOI:10.1175/MWR-D-18-0054.1.

Hong, S.-Y., Y. Noh, and J. Dudhia, 2006: A New Vertical Diffusion Package With an Explicit Treatment of Entrainment Processes. *Mon. Wea. Rev*., **134**, 2318–2341. DOI:10.1175/MWR3199.1.

Hoskins, B. J., I. Draghici, and H. C. Davies, 1978: A New Look at the ω-Equation. *Quart. J. Roy. Meteor. Soc*., **104**, 31–38. DOI:10.1002/qj.49710443903.

Kawashima, M., 2016: The Role of Vertically Propagating Gravity Waves Forced by Melting-Induced Cooling in the Formation and Evolution of Wide Cold-Frontal Rainbands. *J. Atmos. Sci*., **73**, 2803-2836.

Keeler, K. M., B. F. Jewett, R. M. Rauber, G. M. McFarquhar, R. M. Rasmussen, L. Xue, C. Liu, and G. Thompson, 2016a: Dynamics of Cloud-Top Generating Cells in Winter Cyclones. Part I: Idealized Simulations in the Context of Field Observations. *J. Atmos. Sci*., **73**, 1507-1527. DOI:10.1175/JAS-D-15-0126.1.

Keeler, K. M., B. F. Jewett, R. M. Rauber, G. M. McFarquhar, R. M. Rasmussen, L. Xue, C. Liu, and G. Thompson, 2016b: Dynamics of Cloud-Top Generating Cells in Winter Cyclones. Part II: Radiative and Instability Forcing. *J. Atmos. Sci*., **73**, 1529-1553. DOI:10.1175/JAS-D-15-0127.1.

Kenyon, J. S., 2013: The Motion of Mesoscale Snowbands in Northeast U.S. Winter Storms. M.S. thesis, Dept. of Atmospheric and Environmental Sciences, University at Albany, State University of New York, 108 pp., http://www.atmos.albany.edu/student/jkenyon/Kenyon_thesis.pdf.

Martin, J. E., 1998: The Structure and Evolution of a Continental Winter Cyclone. Part I: Frontal Structure and the Occlusion Process. *Mon. Wea. Rev*., **126**, 303–328

Nicosia, D. J., and R. H. Grumm, 1999: Mesoscale Band Formation in Three Major Northeastern United States Snowstorms. *Wea. Forecasting*, **14**, 346–368. DOI:10.1175/1520-0434(1999)014,0346:MBFITM.2.0.CO;2.

Norris, J., G. Vaughan, and D. Schultz, 2014: Precipitation Banding in Idealized Baroclinic Waves. *Mon. Wea. Rev*., **142**, 3081–3099. DOI:10.1175/MWR-D-13-00343.1.

Norris, J., G. Vaughan, and D. M. Schultz, 2017: Variability of Precipitation along Cold Fronts in Idealized Baroclinic Waves. *Mon. Wea. Rev*., **145**, 2971-2992. DOI: 10.1175/MWR-D-16-0409.1

Novak, D. R., L. F. Bosart, D. Keyser, and J. S. Waldstreicher, 2004: An Observational Study of Cold Season–Banded Precipitation in Northeast U.S. Cyclones. *Wea. Forecasting*, **19**, 993–1010. DOI:10.1175/815.1.

——, B. A. Colle, and S. E. Yuter, 2008: High-Resolution Observations and Model Simulations of the Life Cycle of an Intense Mesoscale Snowband Over the Northeastern United States. *Mon. Wea. Rev*., **136**, 1433–1456. DOI:10.1175/2007MWR2233.1.

——, ——, and R. McTaggart-Cowan, 2009: The Role of Moist Processes in the Formation and Evolution of Mesoscale Snowbands Within the Comma Head of Northeast U.S. Cyclones. *Mon. Wea. Rev*., **137**, 2662–2686. DOI:10.1175/2009MWR2874.1.

——, ——, and A. R. Aiyyer, 2010: Evolution of Mesoscale Precipitation Band Environments Within the Comma Head of Northeast U.S. Cyclones. *Mon. Wea. Rev*., **138**, 2354–2374. DOI:10.1175/2010MWR3219.1.

Penner, C. M., 1955: A Three-Front Model for Synoptic Analyses. *Quart. J. Roy. Meteor. Soc*., **81**, 89–91

Petterssen, S., 1936: Contribution to the Theory of Frontogenesis. *Geofys. Publ*., **11** (6), 1–27

Plougonven, R., and F. Zhang, 2014: Internal Gravity Waves from Atmospheric Jets and Fronts. *Rev. Geophys*., **52**, 33–76.

Rauber, R. M., S. M. Ellis, J. Vivekanandan, J. Stith, W-C. Lee, G. M. McFarquhar, B. F. Jewett, and A. Janiszeski, 2017: Finescale Structure of a Snowstorm Over the Northeastern United States: A First Look at High-Resolution HAIPER Cloud Radar Observations. *Bull. Amer. Meteor. Soc*., **98**, 253–269. DOI: 10.1175/BAMS-D-15-00180.1.

Rosenow, A. A., D. M. Plummer, R. M. Rauber, G. M. McFarquhar, B. F. Jewett, and D. Leon, 2014: Vertical Velocity and Physical Structure of Generating Cells and Convection in the Comma Head Region of Continental Winter Cyclones. *J. Atmos. Sci*., **71**, 1538–1558. DOI:10.1175/JAS-D-13-0249.1

Rotunno, R., W. C. Skamarock, and C. Snyder, 1994: An Analysis of Frontogenesis in Numerical Simulations of Baroclinic Waves. *J. Atmos. Sci*., **51**, 3373–3398. DOI:10.1175/1520-0469(1994)051,3373:AAOFIN.2.0.CO;2.

Shields, M. T., R. M. Rauber, and M. K. Ramamurthy, 1991: Dynamical Forcing and Mesoscale Organization of Precipitation Bands in a Midwest Winter Cyclonic Storm. *Mon. Wea. Rev*., **119**, 936–964. DOI:10.1175/1520-0493(1991)119,0936:DFAMOO.2.0.CO;2.

Skamarock, W., J. B. Klemp, J. Dudhia, D. O. Gill, D. Barker, M. G. Duda, X. -Y. Huang, and W. Wang, 2008: A Description of the Advanced Research WRF Version 3. NCAR Technical Note NCAR/TN-475+STR. DOI:10.5065/D68S4MVH.

Thompson, G., P. R. Field, R. M. Rasmussen, and W. D. Hall, 2008: Explicit Forecasts of Winter Precipitation Using an Improved Bulk Microphysics Scheme. Part II: Implementation of a New Snow Parameterization. *Mon. Wea. Rev*., **136**, 5095–5115. DOI:10.1175/2008MWR2387.1.

Uccellini, L. W., and S. E. Koch, 1987: The Synoptic Setting and Possible Energy Sources for Mesoscale Wave Disturbances. *Mon. Wea. Rev*., **115**, 721–729.

Xu, Q., 1992: Formation and Evolution of Frontal Rainbands and Geostrophic Potential Vorticity Anomalies. J. Atmos. Sci., 49, 629–648, DOI:10.1175/1520-0469(1992)049,0629:FAEOFR.2.0.CO;2.

Zhang J., K. Howard, C. Langston, B. Kaney, Y. Qi, L. Tang, H. Grams, Y. Wang, S. Cocks, S. Martinaitis, A. Arthur, K. Cooper, J. Brogden, and D. Kitzmiller, 2016: Multi-Radar Multi-Sensor (MRMS) Quantitative Precipitation Estimation: Initial Operating Capabilities. *Bulletin of the American Meteorological Society*, **97**(4), 621–638. DOI: 10.1175/BAMS-D-14-00174.1